MODELING AND FABRICATION OF SILICON MICRO-GROOVED HEAT PIPES

A THESIS SUBMITTED TO

THE GRADUATE SCHOOL OF ENGINEERING AND SCIENCE

OF BILKENT UNIVERSITY

IN PARTIAL FULFILLMENT OF THE REQUIREMENTS FOR

THE DEGREE OF

MASTER OF SCIENCE

IN

MECHANICAL ENGINEERING

By

Serdar Taze

April, 2015

MODELING and FABRICATION OF SILICON MICRO-GROOVED HEAT PIPES
By Serdar Taze
April, 2015

We certify that we have read this thesis and that in our opinion it is fully adequate, in scope and in quality, as a thesis for the degree of Master of Science.

____
Assist. Prof. Dr. Barbaros Çetin(Advisor)

____
Prof. Dr. Zafer Dursunkaya (Co-advisor)
Middle East Technical University

____
Assist. Prof. Dr. Yegân Erdem

____
Assoc. Prof. Dr. Almıla Güvenç Yazıcıoğlu
Middle East Technical University

Approved for the Graduate School of Engineering and Science:

____
Prof. Dr. Levent Onural
Director of the Graduate School

ABSTRACT

MODELING AND FABRICATION OF SILICON MICRO-GROOVED HEAT PIPES

Serdar Taze
M.S. in Mechanical Engineering
Advisor: Assist. Prof. Dr. Barbaros Çetin
April, 2015

Micro heat pipes (MHPs) are of current interest in the cooling of electronic components due to their high heat removal capacity as a result of the phase change mechanism. This thesis work focuses on finite element modeling and fabrication of a silicon micro-grooved heat pipe system. The computational model is developed to design an MHP system which consists of cooling and heating units and micro-grooves. The 3–D computational model is developed by using the phase change results of a detailed computational model on a unit cell as a boundary condition. Finite element modeling is also used for the design of the cooling channels and the heaters of the MHP system. The 3–D temperature distribution on an MHP system is obtained, and the effects of multiple channels, which cannot be captured by the unit cell analysis are reported. Two different main fabrication techniques, namely lithography-based and mechanical-based, have been assessed for the fabrication of micro-groove structures. For the lithography-based fabrication, deep reactive ion etching together with photo-lithography is used. Many process parameters are tested and optimized to achieve the desired micro-groove structure. According to the tested parameters, a final recipe is prepared and tested on a $< 100 >$ Si wafer. Square micro-grooves with a width and a depth of $200\,\mu$m are obtained for 580 cycle dry etching with grassing formation which is below 5% (acceptable) of the micro-groove height. For the mechanical fabrication, cutting with an automated dicing saw, and high-precision machining with a diamond tool and a PCD tool have been assessed. Satisfactory results have been achieved by the dicing saw. A drawback of the dicing saw technique is the presence of a curve-shaped profile at the beginning and end of the grooves. This study showed the dicing saw to be a fast and cost effective alternative to other techniques. On the other hand, the results of high-precision machining are found to be unsatisfactory for the fabrication of micro-grooves. Moreover, the machining time and the cost of this technique turns out to unfeasible for the fabrication

of a MHP system. The cooling channels are fabricated using PDMS molding, and the chromium heaters are fabricated using photolithography and sputtering. The bonding of the layers of the MHP system is accomplished by plasma treatment. The lithography-based fabrication and the dicing saw techniques are performed at the Bilkent University National Nanotechnology Research Center, and high-precision machining is performed at the Bilkent University Micro System and Design Center.

Keywords: micro heat pipe, micro-groove, silicon, multi-physics modeling, lithography-based fabrication, mechanical-based fabrication.

ÖZET

SİLİKON MİKRO-OLUKLU ISI BORUŞUNUN MODELLENMESİ VE ÜRETİMİ

Serdar Taze
Makina Mühendisliği, Yüksek Lisans
Tez Danışmanı: Assist. Prof. Dr. Barbaros Çetin
Nisan, 2015

Elektronik parçaların soğutulmasında micro ısı boruları (MIB) tercih edilmektedir ve bunun temel nedeni ise faz değişimi sonucu oluşan yüksek ısı çekim kapasitesidir. Bu bağlamda, tez çalışmasında mikro-oluklu ısı borusu sisteminin sonlu elemanlar modellenmesine ve üretimine odaklanılmıştır. Sayısal model kullanılarak soğutucu, ısıtıcı, mikro-oluklardan oluşan bir MIB sisteminin tasarımı tamamlanmıştır. Birim mikro ısı tüpününde yapılan detaylı sayısal faz değişimi analizi sonuçları, 3-boyutlu model oluşturulmasında kullanılmıştır. Soğutucu kanalları ve ısıtı tasarımda da sonlu elemenlar modeli kullanılmıştır. 3-boyutlu sıcaklık dağılımı oluşturulmuş ve birim modelin öngöremediği çoklu kanal etkileri gözlenmiştir. Mikro-oluklu yapı üretimi için iki temel üretim tekniği olan litografi temelli ve mekanik temelli üretim uygulanmıştır. Litografi temelli üretimde, fotolitografi ile birlikte derin reaktif iyon aşındırma uygulanmıştır. İstenen mikro-oluklu yapı için birçok üretim parametresi test ve optimize edilmiştir. Test edilen parametrelere göre reçete oluşturulmuş ve $< 100 >$ Si plaka üstünde fotolitografi işlemi tamamlanmıştır. İstenen kare mikro-oluk derinliği (200 μm) olup, 580 döngü derin reaktif iyon aşındırma ile oluşturulurulmuş, mikro-oluk derinliğinin %5in (kabul edilebilir) den daha az çimensi yapıda gözlenmiştir. Mekanik tabanlı üretimde, otomatik testere dilimleme ile birlikte elmas ve PCD kesici takım ile yüksek hassasiyetli mekanik talaşlı işleme tamamlanmıştır. Otomatik testere dilimleme yönteminde başarılı sonuçlar elde edilmiştir. Bu yöntemin tek olumsuz yönü ise mikro-oluk uç kısımlarında oluşan kavisli profildir. Yapılan çalışmalardan otomatik testere dilimleme yönteminin diğer yöntemlere göre çok hızlı ve düşük maliyetli olduğu sonucu çıkarılmıştır. Fakat, yüksek hassasiyetli mekanik talaşlı işlemenin mikro-oluk üretiminde yetersiz kaldığı görülmüştür. Ayrıca, mekanik talaşlı üretimin MIB üretiminde çok yavaş ve maliyetli olması, yöntemin makul olmadığını göstermiştir. Soğutucu kanallar, PDMS kalıplama ile üretilirken, Cr ısıtıcı fotolitografi ve film kaplama yöntemleri kullanılarak üretilmiştir. MIB sistemi parçalarının birleştirilmesinde plazma uygulaması kullanılmıştır. Litografi temelli üretimler ve testere dilimleme tekniği Bilkent Üniversitesi Ulusal Nanoteknoloji Araştırma Merkezi'nde (UNAM) tamamlanmıştır. Yüksek hassasiyetli mekanik talaşlı işleme ise Bilkent Üniversitesi Mikro Sistem ve Tasarım Merkezinde yapılmıştır.

Anahtar sözcükler: mikro ısı borusu, mikro-oluk, silikon, çoklu-fizik modelleme, lithografi tabanlı üretim, mekanik-tabanlı üretim.

Acknowledgement

I would like to use this opportunity to thank my advisor Assist. Prof. Dr. Barbaros Çetin for his guidance and advice during my thesis.

I express my gratitude to every one who supported me throughout my master study: Prof. Dr. Zafer Dursunkaya, Dr. Mehmet Yılmaz, Dr. Gülnihal Odabaşı, Mrs. Soheila Zeinali, Mr. Semih Yaşar, Mr. Mustafa Kılıç, Mr. Samad Nadimi, Mr. Serhat Kerimoğlu, Mr. Ersin Hüseyinoğlu, Mr. Hossein Alijani and Mr. Stefan Ristevski. I am grateful to them for helping and sharing their illuminating views.

I would like to thank my mother (Gülse), my father (Celal), my brother (Mustafa) and my sister (Sinem) for supports throughout my life.

Additionally, I am grateful to Microfluidics & Lab-on-a-chip Research Center, National Nanotechnology Research Center, Advanced Research Laboratories and Micro System Design and Manufacturing Center to share their facilities.

I would also thank the Turkish Scientific and Technical Research Council (TÜBİTAK) for the financial support for my thesis through the project of 213M351.

Contents

List of Figures

List of Tables

Chapter 1

Introduction

New technological devices such as tablet computers, smart phones or other applications have become widespread for daily usage during the last decade. The main reason behind this improvement is the development in the microchip and integrated circuit technology. Especially, the capabilities and performance of the microchips has increased dramatically in recent decades, which brings new opportunities to produce multipurpose small scaled electronic devices for daily use. Although these technological developments are scaling down the size of the chips with increased performance, there are still two limiting factors for further improvements, namely challenges in fabrication and overheating of microchips which can cause malfunctioning and/or reduced life time. Many researchers have been working to overcome these problems. Considering fabrication side, there is not much to do, since the present techniques are very standardized and there is no novel technique commercially feasible. Therefore, the major contribution to improve the performance of the microchips can be performed by using efficient cooling techniques and reducing temperature rise of the components. Operating at elevated temperature reduces life time of the microchips; therefore, the efficient cooling of the system the bottleneck. Regarding this issue, some cooling methods have been proposed such as thermoelectric cooling, direct immersion pool boiling, heat pipes, spray cooling (liquid jet impingement), and forced convective boiling [5] (the detailed information about thermoelectric cooling [6], direct immersion

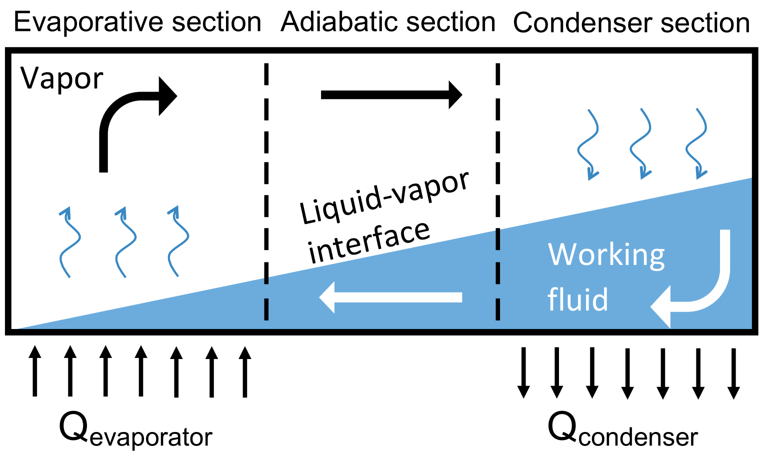

Figure 1.1: Working schematic of heat pipe

pool boiling [7], spray cooling (liquid jet impingement) [8], and forced convective boiling [9] can be found elsewhere). The main idea behind aforementioned methods is the benefit of phase change phenomena, since a large amount of thermal energy is absorbed or released from the working fluid to the environment during the phase change process.

Many mathematical and experimental studies have been conducted in the aforementioned methods to characterize and quantify the thermal performance more specifically the heat removal capacity. Although satisfactory heat removal has been reached by many of the cooling processes, heat pipe is the most promising cooling method due to their unique advantages namely **(i)** simplicity, **(ii)** no additional component requirements, **(iii)** less amount of working fluid and **(iv)** high heat flux removal capacity. Therefore, heat pipes are the common choice by many researchers and companies who are dealing with high heat generating electronic devices [5]. To have a better understanding about heat pipes, the working principle can be explained as the transfer of heat from one solid interface to another which are evaporator and condenser sections. Heat flux is applied to the evaporator region with a heat source, which vaporizes the working liquid. The vaporized liquid is transported to the condenser region. At the condenser region, vaporized liquid condenses by the removal of heat flux though heat sinks. The condensed liquid moves through the evaporator region with the help of the gravity, centrifugal and/or capillary forces (among these capillary is the most common one and in fact the most dominant parameters in the performance of the heat pipe [10]). This process repeats itself naturally and the circulation of heat and fluid is obtained inside a heat pipe. The working simulation of a heat pipe is represented in Figure 1.1. The detailed information about the historical development of the heat pipes was given by Suman [10].

1.1 Operational Limits of Heat Pipe

The operational limitations of heat pipes restrict the further improvements for the performance and capability. The limitations are generally observed during the operation of the heat pipe by measurements and visualizations. The limitations can be characterized in two main categories. One category is the limitations causing the failure of the heat pipe due to inadequate flow of working fluid to evaporator section which may cause dry-out [11]. These limitations are capillary, boiling and entrainment limits. Second category is the limitations not causing the failure of the heat pipe which are sonic and viscous limits. In the second category of limitations, the heat pipe can operate at increased temperatures for increased heat inputs. Different limitations are discussed in details in the upcoming subsections.

1.1.1 Capillary limit

The fluid flow within a heat pipe is generated naturally mainly due to the capillary pressure difference across the liquid-vapor interfaces [12]. The shape of the liquid-vapor interface relies on two forces which are liquid's surface tension and solid-liquid adhesion forces which are the forces between different substances. The movement between solid-liquid interface within small containers is called as capillary action [11]. In heat pipes, this phenomena created by wick structures placed inside a heat pipe. In normal operation conditions of heat pipes, the capillary pressure difference must be greater than the total pressure loss inside a heat pipe. Otherwise insufficient liquid flow from condenser section to evaporator section is observed which causes the dry-out of the liquid at the evaporator section due to insufficient capillary forces. The capillary pressure is defined by Young-Laplace equation and the two principal menisci radii of curvature (R_I, R_{II}) are the primary sources of the capillary pressure:

$$P_c = \sigma \left(\frac{1}{R_I} + \frac{1}{R_{II}} \right) \tag{1.1}$$

where σ represents the surface tension between two fluids.

The total pressure loss can be divided into three part. Frictional pressure drop in the liquid phase (ΔP_l) that helps the liquid flow from condenser to evaporator. The other pressure loss is the frictional pressure drop in the vapor phase (ΔP_v) that helps the vapor flow from evaporator to condenser. The last one is due to the body forces mainly gravitational head and the inclination of a heat pipe which determines the effect of pressure loss. This loss can be positive, negative or zero. The capillary limitation becomes important when the capillary forces are less than the total pressure loss. In the case of dry-out at the evaporator, the fluid flow stops and so does the heat transfer from evaporator to condenser which results in the failure of the operation of the heat pipe. Therefore, to satisfy the normal operation of heat pipe, the capillary pressure should be larger than the pressure losses. This relation can be formulated as:

$$\Delta P_c > \Delta P_l + \Delta P_v + \Delta P_b \tag{1.2}$$

1.1.2 Viscous limit

The operation temperature of heat pipes has significant effect on the performance of a heat pipe; however, it does not cause any failure of the system. When the operation temperature of a heat pipe is low, the vapor pressure at the evaporator section may not be enough to carry the vapor from evaporator to condenser. This low-flow of vapor is called as viscous limit. For viscous limit, the total vapor pressure is compensated by the viscous forces in the vapor channel. The viscous limit is generally observed in longer heat pipes due to the low vapor pressure within the channels when the working fluid is close to its melting temperature or observed when the working fluid is frozen [12]. The heat input can be increased to overcome the viscous limit; however, in over heating of a heat pipe, the sonic limit may be realized.

1.1.3 Sonic limit

The sonic limit is observed during the start-up or low operating temperature of the liquid-metal heat pipes. The main reason is the very low vapor density in the heat pipe; therefore, sonic (or choked) vapor flow is observed. The typical heat pipes working in room temperature or cryogenic temperatures, the sonic limit is not significant except for very small vapor channel diameters. Dry-out or failure of the heat pipe is not observed due to the sonic limit, however it limits the axial heat transport capacity. If the sonic limit surpassed, the evaporator temperature and axial temperature gradient along the heat pipe increases which leads to decrease in the isothermal behavior in the vapor flow region [12].

1.1.4 Entrainment limit

For heat pipes operating at ideal conditions, the vapor and liquid flows in counter direction which causes viscous shear forces at the liquid-vapor interface. If the interfacial shear force becomes dominant on the liquid surface tension force, the liquid droplets can be carried out to the condenser by the vapor. Therefore, insufficient liquid flow from the condenser to the evaporator within the wick structure occurred and as a result dry-out of the liquid in the evaporator is observed [12]. The entrainment limit can be estimated by using the non-dimensional Weber number [13].

1.1.5 Boiling limit

The boiling limit becomes effective when the heat flux exceeds the critical heat flux in the evaporator that is why nucleate boiling occurs within the wick structure and bubbles are generated. If the bubbles grow, they may trapped in the evaporator and blocks the liquid flow through the evaporator and dry-out is observed which stops the operation of heat pipe [13]. This phenomenon called boiling limit and it directly depends on the radial and/or circumferential heat flux. Due to the fact that the bowling limit depends on high heat flux, it is also indicated as the heat flux limit [12].

1.2 Micro Heat Pipe

After many years of proposition of heat pipes, the idea of micro heat pipe (MHP) was first introduced by Cotter [14] in 1984, and extensively studied to understand the performance parameters and improve the performance of MHPs. MHP is a micro-scale heat pipe used to transferring heat from heating to cooling section. Typically, MHPs contain long, thin and non-circular channels with sharp corners which work as a liquid artery. The commercial MHPs are generally preferred and used in strategic industries like defense and space. However, some new applications more on the civil industries such as cooling of memory chips, CPU, LED TV, automobile LED head lamp and LED lighting has been realized by the researchers [15]. Cotter [14] defined MHPs as the heat pipes with small channels which has mean curvature radius of vapor-liquid interface distinguishable in magnitude wise with hydraulic radius of flow channels. Depending on the different operating conditions and applications, different working fluids, geometries and materials have been considered for MHPs.

1.2.1 Working Fluids and MHP Materials

The regular cooling systems (i.e. air conditioners), heat exchangers or heat pipes use special or regular working fluids depending on the operating conditions. The working fluids are water, acetone, methanol, n-Pentane, toluene, helium, R-11, R-12, R-22 and R-134 etc. The selection of the working fluid depends on some critical parameters, namely [16]:

- Convenient and wettable with wick and wall material,
- high thermal conductivity and latent heat,
- high surface tension and low liquid & vapor viscosity,
- thermally stable and tolerable freezing and pour point,
- the vapor pressure depending on the operating temperature.

The working fluid should have good wettability characteristics on wick structure to improve evaporation. A high latent heat of working fluid is also desirable for more effective heat transfer with low fluid flow. Moreover, high thermal conductivity reduces the radial temperature gradient and probability of nucleate boiling at wick-wall interface. Surface tension of the working fluid should be high to generate large capillary forces and helps work against the gravity. The stability of working fluid especially for some organic fluids is crucial to prevent any separation of components of fluid; therefore, the film temperature should be maintained under a specific value. Additionally, the vapor pressure should not be lower than a certain value, otherwise high vapor velocity causes large temperature gradient or unstable flow. Moreover, high vapor pressure, which means most of the liquid is evaporated, requires an additional thick-walled liquid container [16].

The selection of the working fluid is very crucial on the performance of the heat pipes since the heat transport capacity is directly related with working fluid; therefore, a non-dimensional number has offered as an indicator in the selection

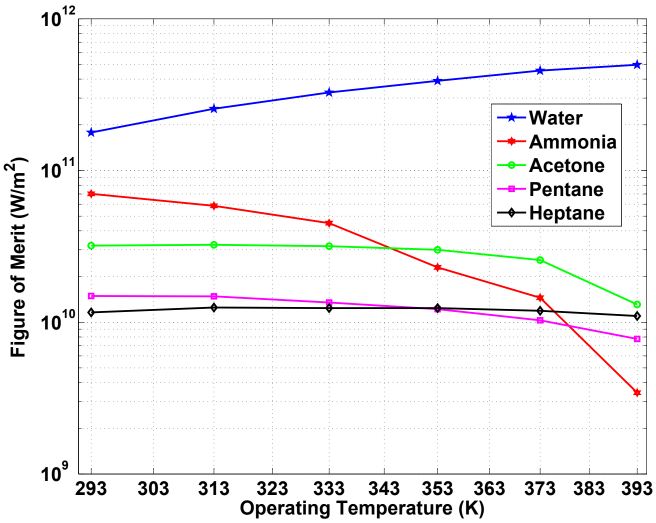

Figure 1.2: Figure of Merit number of candidate heat pipe working fluids for intermediate temperatures -y axis logarithmic scaled- (Adapted from [1])

of the working fluid [1]. This number described as Merit number (Me) which strongly depends on thermo-physical properties of working fluid [17] :

$$Me = \frac{\sigma_l \rho_l L}{\mu_l}, \tag{1.3}$$

where σ is the surface energy per unit area of liquid, ρ_l is the density of liquid, L is the latent heat of vaporization, and μ_l is the dynamic viscosity of liquid. To reach optimum operation conditions of the heat pipe, the Merit number needs to be maximized. For different working fluids, the variation of Figure of Merit with temperature is represented in Figure 1.2 where Figure of Merit is a quantity to describe the performance of devices or system and also used as a marketing tool. For the operation temperatures ranges between 293 K and 393 K, except for water, other working fluids shows decrease in Me as a result decrease in heat transport capacity with increasing operation temperature. Water demonstrates substantial increase in Me with increase of operation temperature; therefore, water is the most selected principal working fluid in heat pipes [1]. It can also be observed that the effect of operation temperature on Me is negligible for heptane.

The commonly used working fluids in heat pipe systems together with range for the operation temperature have been well established [16]. Considering MHPs, the proper working fluids are generally pure water when the operation conditions and materials of the MHP are considered. The selected working fluids in MHP systems were listed by Sobhan [18] for the studies until 2005. More recent summary about the working fluids is given in Table 1.1. Until 2005, the most common working fluids were water, methanol (which is mostly used with silicon MHP), n-Pentane, ethanol and ammonia. However, although methanol, ethanol, n-Pentane, ammonia, acetone, FC-72 and R113 were also preferred, the tendency of the working fluid has been towards pure water as seen from Table 1.1.

More recently, different mathematical models have been developed to understand the effect of the working fluid on the thermal performance of MHPs. Liu et. al. [19] developed a transient mathematical model to see the effect of the working fluids (methanol, ethanol, acetone, ammonia) on the start-up time. They also validated their model with experimental results. They observed that ethanol exhibits the fastest start-up time whereas methanol the slowest. The effect of working fluids (water, ammonia, heptane, ethanol and methanol) on the heat transfer capacity for the range of operating temperatures ($20 - 100°C$) was also studied, and found that ammonia has a better heat transport capacity below 50°C whereas water has a better heat transport capacity above 50°C [20]. Moreover, some studies also considered the inclusion of nanoparticles (CuO), and it is observed that with some optimal nanoparticle concentration, the thermal performance of a MHP can be improved [21, 22]. The effect of the working fluids (pure water, ethanol, FC-72 and R-113) on start-up time of the pulsating silicon MHP are also analyzed [23] and it is observed that FC-72 and R-113 exhibits a start-up time of approximately 200 seconds due to their low dynamic viscosity, low surface tension, low latent heat and high dP/dT_{sat}.

The selection of the MHP material is important which needs to compatible with the working fluid. Additionally, ease of fabrication and the effect on the thermal performance is also another concern. Although there are several options for the fabrication of heat pipes, the fabrication may be challenging considering MHPs due to the micro level structures. To overcome these challenges, many studies have been used copper or silicon as the MHP material as seen from Table 1.1. Both copper and silicon have a high thermal conductivity, and hence results in better thermal performance for the MHP. Recently, the effect of the MHP material on the thermal performance has also studied [17].

1.2.2 MHP Geometries

MHPs with different cross-sections have been studied in the literature. Preferred geometries are summarized in Figure 1.3. The triangular shape was proposed for the first time by Cotter [14] in a theoretical study related to the determination of the maximum heat transfer capacity of a micro-groove. Rectangular shape with straight or incurved sides, square shape with straight sides, trapezoidal shape, circular shape with incurved walls, triangular cross-section with concave walls have been also included [2]. There are also heat pipes having micro-grooves or micro-channels with different cross-sections on flat plates or cylindrical tubes. The selected cross-section by researchers can be listed as rectangular, triangular, trapezoidal, star shaped, and rectangular grooves on tubular structure. The selected MHP geometries were listed by Sobhan [18] for the studies until 2005. More recent summary about the geometry of MHPs together with the size of the channels is included in Table 1.1. From Table 1.1, the most commonly selected channel geometry is rectangular due to the ease of fabrication. In the selection of the channel size, generally manufacturing capabilities and filling of working fluid to micro-grooves are taken into account.

In conventional heat pipes, capillary pressure difference that is main driven force of liquid working fluid from condenser to evaporator, which is created with the wick structure. However, in MHPs, the essential capillary pressure difference ensured with the sharp-edged channels or grooves [24]. The sharpness of the edges of the channels has a vital role in operation of MHPs. The number of corners in regular polygonal shapes directly effects the sharpness of the edges. Increase in the corners of polygon increases the corner apex angle; therefore, as the sharpness of the edges decreases, the capillary pumping ability also reduces [25]. Consequently, triangular and V-shaped MHPs have also been considered [11]. Moreover, it was observed that star-groove MHPs exhibit an outstanding capillary

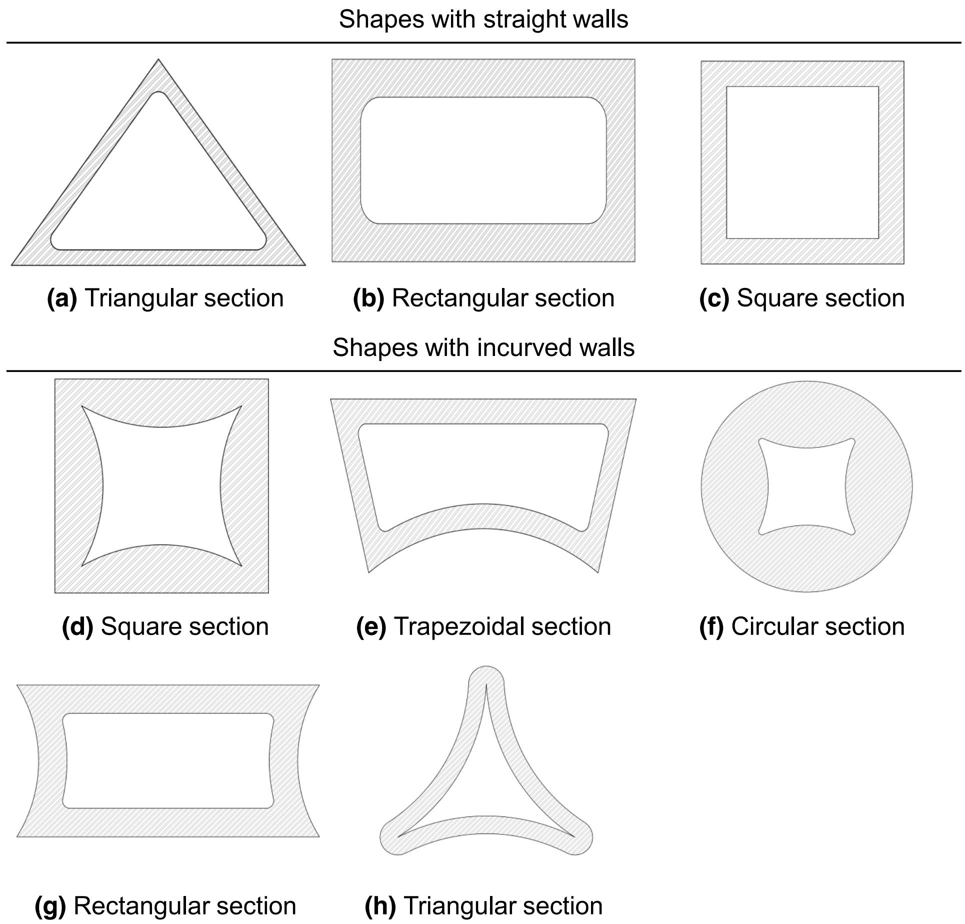

Figure 1.3: Preferred MHP micro-groove cross-sections (Adapted from [2])

pumping performance since the corner apex angle can be arranged to desired value to obtain the sharp corners without changing the number of corners in geometry [25]. Although the star-groove MHPs have significant capillary pumping ability as a result of a good heat transport capacity, the fabrication of the pipe is challenging; therefore, more simple geometries such as rectangular, square and triangular are more common.

1.2.3 Fabrication Techniques

The main start-up point for the experimental work on MHPs is the fabrication of a MHP. The precesses of fabrication includes many important parameters such as channel sizes, shape of cross-section of channel, number of channels, MHP material. The listed parameters are determined according to heat removal rate, working fluid, working parameters such as filling ratio, operation temperature range. Generally preferred fabrication techniques depend upon the available material and simplicity of the fabrication processes. The common tendency in fabrication on silicon wafer is wet etching due to its simplicity and easy access. For the copper MHP, machining techniques have been also used for the fabrication. The preferences in recent studies can be seen in Table 1.1. There are several machining techniques used in fabrication which are laser micro-machining, milling and extrusion-ploughing.

1.2.4 Heating and Cooling Processes

Heating and cooling of a MHP is a crucial step for the experimentation. The size, heat removal and/or supply rates are the design parameters of the heater and cooler which are determined by the researchers. Generally, the heater is chosen as resistive electric heater which generate heat due to that electrical current passes through electrical resistor transferring the electrical energy to heat energy [26, 27, 21, 28, 22, 29, 30, 31, 32, 23, 33, 34]. The heat input given by heater is calculated by multiplying electrical potential (V) with electrical current (I). By controlling the input voltage, the desired heating power can be achieved. There is small differences in cooling methods. The main concept in the cooling is circulating water in heat sink and it is preferred by many groups [27, 22, 29, 30, 31, 32, 23, 34]. Addition to water heat sink, cooling fan [21], water reservoir [26], ambient air [33] and refrigerant bath circulator [28] have also been used for cooling purpose. The summary of heating and cooling methods used in the experimental studies is given in Table 1.2 and it can be realized that electrical resistance heaters are commonly used due to the ease of fabrication, small size and the ease of control. The only difference between these heating techniques is the heater configurations which may be either wire or film heaters.

Table 1.1: Comparison of different MHP systems

Reference	Channel geometry/size	Fabrication technique and material	Working fluid
[26]	Rectangle / W: $200, 300, 500\,\mu$m, H: $200, 300, 500\,\mu$m	Chemical etching and precision milling on copper plate	Pure water
[21]	Rectangle / W: $500\,\mu$m, H: $800\,\mu$m	** & copper plate	Pure water with CuO nanoparticles
[35]	Trapezoid / W: $262\,\mu$m, H:$195\,\mu$m	Copper plate (Mathematical model)	Pure water
[28]	Fan-shaped (V) / W: $150\,\mu$m, H: $300\,\mu$m	Laser micro-machined copper plate	Pure water
[36]	Rectangle / W: $200\,\mu$m, H: $420\,\mu$m, W: $203\,\mu$m, H: $839\,\mu$m	Copper plate (Mathematical model)	Pure water
[22]	Rectangle / W: $250\,\mu$m, H: $200\,\mu$m	** & copper plate	Pure water with CuO nanoparticles
[37]	Equilateral triangle / W: $300\,\mu$m	**	No information
[20]	Equilateral triangle / W: $1000\,\mu$m	** (Mathematical model)	Water, heptane, ammonia, methanol, ethanol
[29]	Rectangle / W: $400\,\mu$m, H: $380\,\mu$m	Machining on copper plate	Methanol
[38]	Rectangle (on tube) / W: $240\,\mu$m, D: $150\,\mu$m	Extrusion-ploughing process on copper	Acetone
[31]	Rectangle / W: $400\,\mu$m, H: $400\,\mu$m	Machining on copper plate	n-Pentane
[30]	Rectangle (radially oriented)	Etching on silicon wafer	Methanol
[39]	Equilateral triangle / W: $1040\,\mu$m W: $200\,\mu$m, H: $420\,\mu$m, W: $203\,\mu$m, H: $839\,\mu$m	Copper, nickel and monel (Mathematical model)	Pure water
[25]	Star-groove (4, 6, 8 corners), equilateral triangle	Silicon (Mathematical model)	Pure water
[32]	Rectangle / W: $400\,\mu$m, H: $400\,\mu$m	Machining on copper plate	n-Pentane
[40]	Equilateral triangle / W: $1040\,\mu$m	Copper (Mathematical model)	Pure water
[23]	Trapezoid (pulsating) / D_h: $251, 352, 394\,\mu$m	Wet etched silicon plate	Water, ethanol, FC-72, R-113
[19]	Equilateral triangle / W: $300, 500, 700\,\mu$m	** (Mathematical model)	Methanol, ethanol, acetone, ammonia
[33]	Rectangle / W: $150\,\mu$m, H: $300\,\mu$m	Extrusion and drawing on copper plate	Pure water
[34]	Sintered wick and trapezium-grooved wick tubular / Trapezium W: $300\,\mu$m, D: $250\,\mu$m	High speed spinning and drawing of copper tube	Pure water
[41]	Equilateral triangle / W: $1040\,\mu$m	Copper and nickel (Mathematical model)	Pure water

** No fabrication information, W:Width, H:Height, D:Diameter, D_h:Hydraulic diameter

Table 1.2: Experimental techniques for different MHP work

Reference(s)	Heating method	Cooling method	Measurement techniques
[26]	Tungsten wire resistance heater	Water reservoir	n-type poly-Si integrated thermistors, T-type thermocouple
[21]	Cartridge electric heater	Cooling fan	Thermocouple, pressure transducer for steam pressure
[27]	Thick resistor film	Water flowing heat sink	Thermocouples and thermistors, Confocal microscope for radius of meniscus curvature
[28]	Nichrome resist-wire heater	Refrigerating bath circulator	K-type thermocouple
[22]	Electrical heater	Cooling water circulating in thermal bath	T-type thermocouple, Pressure transducer for operating pressure
[29]	Thick resistor film	Water flowing heat sink	Thermistors, Confocal microscope for radius of meniscus curvature
[31, 32]	Heated copper block	Water flowing heat sink	Thermocouples and thermistors Confocal microscope for radius of meniscus curvature
[30]	Circular thick resistor film	Water flowing heat sink	T-type thermocouple on kapton film, Confocal microscope for radius of meniscus curvature
[23]	Film heater	Cooling water circulating in cold bath	T-type thermocouple, CCD camera to record two phase flow pattern
[33]	Heating roods heats water bath	Ambient air	K-type thermocouple, IR camera used for overall temperature distribution on MHP
[34]	Electrical bars heats the copper sheathing	Cooled with water	**

** No infromation

1.2.5 Measurement Parameters

The measurement parameters play significant role in the determination of the performance of MHPs. The measurements highly depend on the available measurement devices; therefore, temperatures on the MHP wall, pressure inside the MHP, filling ratio of working fluid and given heating power to MHP by the electrical heater are commonly measured. For temperature measurements, thermocouples (n-,T- and K-type) and thermistors are typically mounted onto the system. Before the work at real conditions of MHP, the calibration of the equipments are completed at non-working condition of MHP. For power supplied to system is calculated by potential difference and the electrical current that can be controlled and monitored with a power supply. Filling rate is determined by dividing the volume of applied working fluid inside the MHP channels with total volume of the inside of MHP which can be calculated with known dimensions and geometry of the channels and the other spaces. Pressure transducers are placed into the working area of the MHP to obtain the steam pressure of the system [21]. In addition to those parameters, meniscus radius of curvature (r) is collected by using confocal microscope [27, 29, 30, 31, 32]. CCD camera has been offered to obtain the two phase fluid flow and boiling inside the channel of MHP [26, 23]. Furthermore, the collected images can be used for the determination of some parameters of the MHP. Infrared (IR) camera is proposed to capture the temperature distribution along the heat pipe wall [33]. The purposes in choosing the IR camera are the accuracy of the camera and the benefit of non-contact measurement technique of temperature. The experimental works on the MHP can be compared with using Table 1.2 in terms of heating & cooling methods and measurement devices. In addition to heating and cooling region as explained, most of the MHP contains adiabatic region between heating and cooling section and its sizes determined according to sizes of the heating and cooling sections.

The MHPs performance under the working conditions, temperatures are commonly measured with thermocouples and thermistors as indicated in Table 1.2. Moreover, if it is available, the types of thermocouples are shown and generally T-type and K-type of thermocouples are preferred due to low prices and high sensitivities. In addition to temperature measurement, the radius of curvature of the working fluid are observed with confocal microscope because the measured radius is used to calculate the capillary pressure difference along the MHP micro-grooves.

1.3 Objectives and Motivation of the Thesis

Although computational modeling has advanced over the decades, the modeling of phase change is still a challenging problem. In the assessment of the thermal performance of a heat pipe, modeling of the phase change is a critical step. Moreover, on top of the modeling of the phase change (evaporation and condensation), a rigorous 3-D modeling of a MHP requires the modeling of fluid flow, convective and conductive heat transfer within MHP. This kind of modeling is computationally extremely expensive. Recently, a rigorous modeling for a single micro-groove (i.e. on a unit cell–which will be called as Unit-Cell-Model (UCM) hereafter) in which the 3–D heat transfer process in the solid and working fluid coupled with a 1–D analysis of momentum equation has been performed [11]. The objective of the present study is to develop a 3–D computational model to assess the thermal performance of a micro-grooved heat pipe (MGHP) which uses the results of UCM as a convective heat transfer boundary condition at the channel wall for the modeling of phase change occurring within the micro-grooves. Since the todays' integrated circuit technology depends on silicon wafers, an efficient cooling of an electronic circuit may be realized by designing a MHP system on a silicon wafer. Therefore, silicon is selected as the MHP material. Within the scope of this study, different fabrication techniques for the fabrication of the silicon micro-groove heat pipe has assessed. Using the developed computational model, a complete MHP system together with the necessary cooling and heating section has been designed and fabricated. The presented MHP system will be used to verify the UCM experimentally. Following the successful verification of the UCM, the proposed computational model will enable researchers to design micro-groove MHP system for the cooling of realistic electronic circuit architecture.

Chapter 2

Design of the MHP System

In this chapter, a 3–D computational model is developed to assess the thermal performance of the silicon-based MHP together with the design of the heating and cooling units. The phase change occurring within the micro-groove is included in the model as a convective heat transfer boundary condition at the micro-groove wall. The evaporator and condenser section heat transfer data are obtained from a detailed computational model on a unit cell [11]. The system is studied to determine the temperature distribution and the effect of parameters such as electrical potential on the Chromium (Cr) heater, channel size of heat sink and water flow rate within the cooling channels by using commercial finite element software COMSOL Multiphysics. The silicon MHP system is designed based on the simulations. The CAD model of the MHP system used in the simulations can be seen in Figure 2.1.

The heat pipe is placed on a standard silicon substrate due to the ease of fabrication of micro-grooves. Moreover, this silicon MHP system is planned to be utilized for the cooling of an IC circuit architecture. The proposed MHP system can be integrated on silicon IC circuits without requiring sealing or bonding processes, and without any treatment for thermal contact resistance. The selected silicon wafer is standard and most commonly used in the micro/nano scaled devices. It has a thickness of $525\,\mu$m with orientation of $< 100 >$ and a diameter

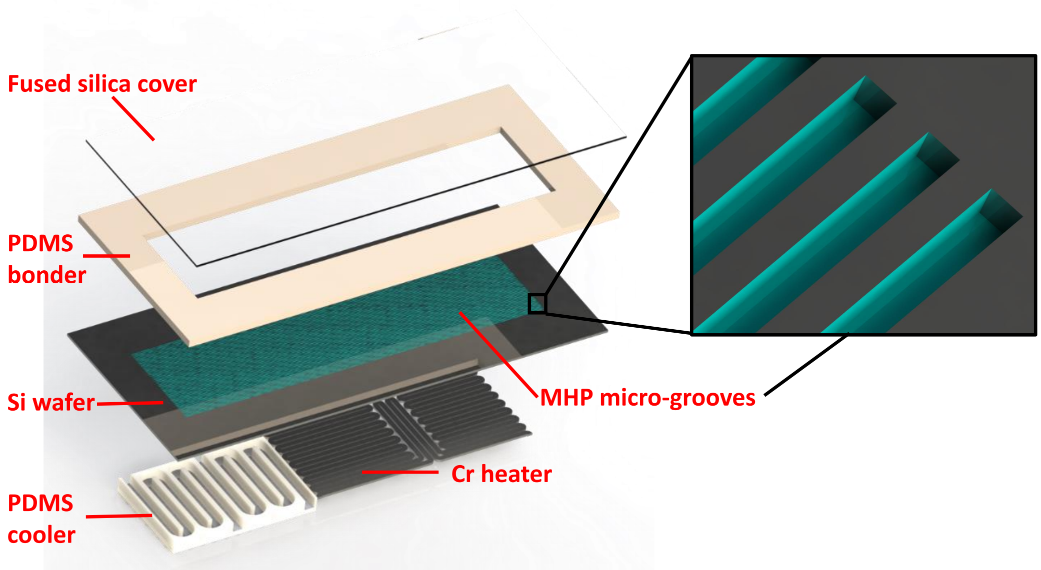

Figure 2.1: CAD model of the MHP system

of 4'' (full wafer). The width and depth of the micro-grooves are selected as $200\,\mu\text{m} \times 200\,\mu\text{m}$. The reason for the selection of this dimension is for the ease of fabrication. Especially, considering the mechanical-based fabrication techniques, although cutting tools with a size smaller than $200\,\mu$m are available, cutting process with such small tools may be problematic. For the height of the micro-grooves, there are two limitations. If the depth of the micro-groove is small, then the amount of working fluid becomes smaller, and the precise control during the loading of the working fluid may become challenging. If the height is too large, then there is a high probability of cracking the wafer during the handling (recall the total height of the wafer is $525\,\mu$m). Therefore, an optimum groove height of $200\,\mu$m is selected. 50 micro-grooves are placed on top of the silicon wafer as shown in Figure 2.1. Upper limit for the number of grooves comes from the geometric limitations, and the lower limit comes from the amount of working fluid to be loaded. If the number of micro-grooves is small, the required volume of the working fluid decreases, and the precise filling of the heat pipe may be problematic at the experimentation stage. Therefore, the number of micro-grooves is selected as 50. Once the computational model is developed, a similar procedure can be applied for any groove dimensions and any number of grooves.

The system consists of silicon wafer, cooling channels embedded in Polydimethylsiloxane (PDMS), deposited Cr heaters and fused silica cover at the top as shown in Figure 2.1. The Cr heaters serve as the evaporator, cooling channels serve as the condenser. The transparency of fused silica will enable the visual inspection of the working fluid during experimentation. The PDMS bonder (spacing) is also located between the silicon wafer and the fused silica cover that is chosen to attach fused silica to silicon wafer, and form a space for the circulation of evaporated working fluid. The cooling channels are also embedded in PDMS. PDMS is selected for the ease of bonding with silicon and fused silica. The computational domain consists of the heat pipe section (with 50 micro-grooves on the top of the wafer), the Cr heater and the cooling section placed at the bottom of the wafer. Micro-grooves are located at the center of the silicon substrate, resulting in a total width of 20 mm. The lengths of the evaporator and condenser sections are $L_e = 45.75\,\text{mm}$ and $L_c = 29.25\,\text{mm}$, respectively.

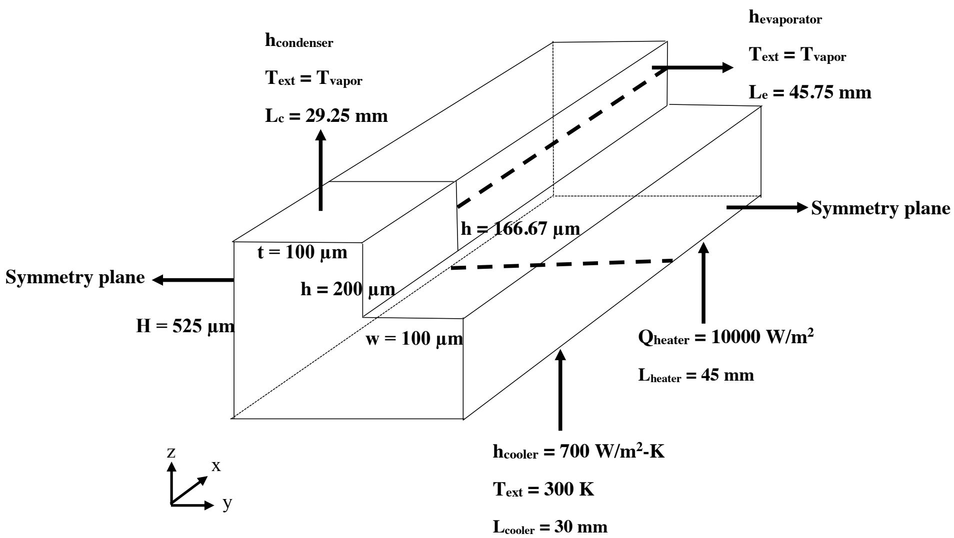

Figure 2.2: UCM and boundary conditions implemented

Table 2.1: Coefficients of two-term exponential curve fit

Section	Functional form	Parameters	Value
Condenser (h)	$a_c \times \exp(b_c x) + c_c \times \exp(d_c x)$	a_c b_c c_c d_c	-2.928×10^9 1456 3.009×10^4 -5.557
Evaporator (h)	$a_e \times \exp(b_e x) + c_e \times \exp(d_e x)$	a_e b_e c_e d_e	6.772×10^{-5} -2550 1.513×10^4 2.067

2.1 Unit-Cell-Model and Simulation Procedure

The phase change heat transfer coefficient data necessary for the evaporator and condenser sections are extrapolated from a coupled model which requires the micro-groove size and other physical parameters for the calculation of heat fluxes, heat transfer coefficients, temperature distribution along the MHP and the mass transfer rate during phase change. The computational domain of the UCM together with the implemented boundary conditions can be seen in Figure 2.2. The heat transfer coefficient data obtained from the UCM are fed into the 3–D model [42]. To implement the phase change, a two-term exponential curve is fit for the local heat transfer coefficient along a micro-groove. The coefficients of two-term exponential curve fit for evaporator and condenser sections are listed in Table 2.1.

Figure 2.3 presents the variation of convective heat transfer coefficient together with the fitted curves and temperature distribution along a unit cell (with a length of 75 mm). The side view of the unit cell is drawn and heat transfer coefficients at evaporator, condenser and cooler sections with the temperatures and heat transfer rate at heater are also represented in Figure 2.4. To validate the use of curve fitted data, the computations are performed on a unit cell and compared with the results of UCM using COMSOL Multiphysics. The temperature variation at the top edge of the micro-groove wall where the majority of phase change occurs [?], is plotted in Figure 2.5. The matching between the temperature profiles for models can be seen which justifies the use of curve fitted data.

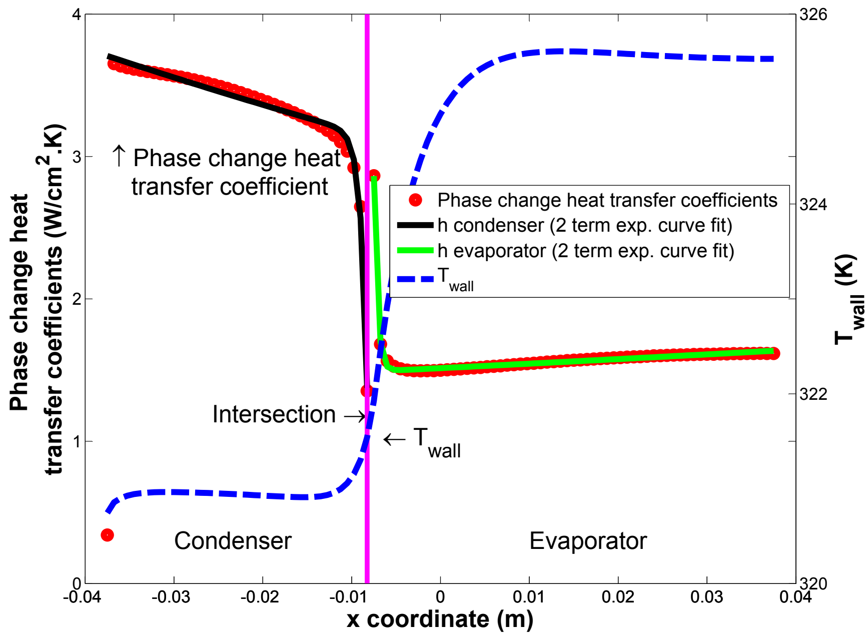

Figure 2.3: Phase change heat transfer coefficients along the unit MHP groove

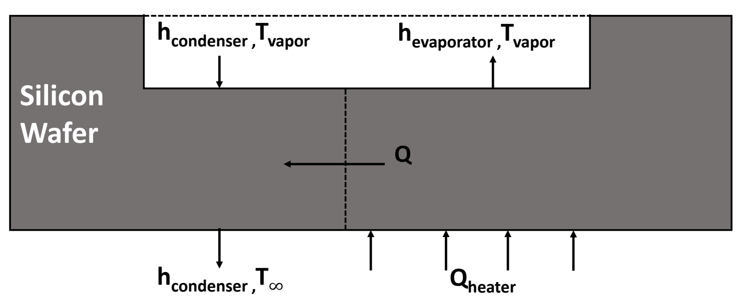

Figure 2.4: Boundary conditions on the unit cell (side view)

2.2 Design of the Cooling Channels

In UCM, the thermal boundary condition at the condenser section was constant convective heat transfer coefficient and constant ambient temperature. Since our proposed system will mimic the conditions in UCM, the cooling channels need to

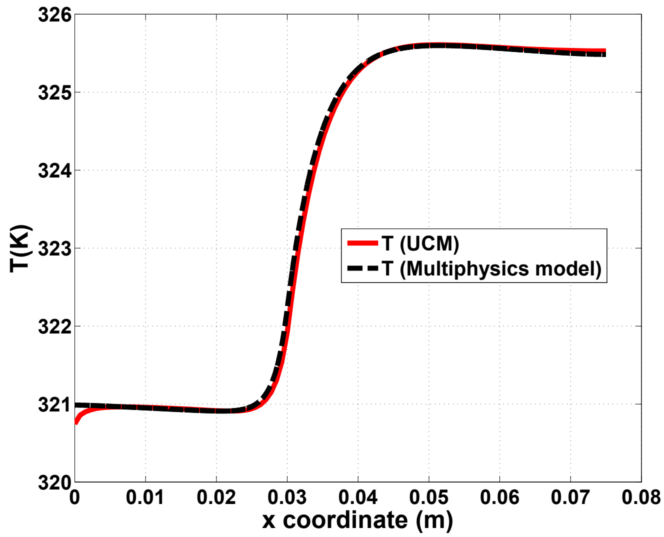

Figure 2.5: Temperature distribution on the unit cell

be designed to match the aforementioned boundary condition. The heat transfer coefficient data from UCM is valid if and only if the specified heat transfer is rejected from the condenser section. Therefore, at this point, the flow conditions and the channel geometry also needs to satisfy the required heat transfer rate and the heat coming from the heater should be transferred to the water, otherwise the temperature at the condenser section may be different than the value predicted by the UCM. Several cooling channel geometries are assessed to obtain the desired heat transfer. The detailed computation of fluid flow and heat transfer requires a detailed mesh to resolve the boundary layers. Assigning fully-developed conditions for fluid flow and heat transfer is physically meaningful; however, assigning fully-developed temperature is problematic from computational point of view. Therefore, instead of solving momentum and energy equation within the cooling channels, convective heat transfer coefficient is assigned at the channel wall which eliminates the computation of flow and temperature field. The necessary heat transfer coefficients are estimated using the appropriate fully developed Nusselt number (Nu) value for constant wall temperature thermal boundary condition. Constant wall temperature is used since the temperature in the condenser region is approximately constant. The water flow in the cooling channels is fully-developed since before entering the PDMS cooling channels, the cooling water

Cross Section	$\frac{b}{a}$	$Nu = \frac{hD_h}{k}$ (Uniform q_s'')	(Uniform T_s)
	---	4.36	3.66
	1.0	3.61	2.98
	1.43	3.73	3.08
	2.0	4.12	3.39
	3.0	4.79	3.96
	4.0	5.33	4.44
	8.0	6.49	5.60
	∞	8.23	7.54
Heated / Insulated	∞	5.39	4.86
	-	3.11	2.49

Figure 2.6: Laminar flow Nu for different cross-sections (Adapted from [3])

supplied from the syringe pumps, passes through a long piping system that ensures that the flow is close to being a fully-developed. In the laminar flow regime, fully-developed Nu is constant and it is not a function of Re (the fully-developed, laminar flow Nu for different cross-sections are given in Figure 2.6). Therefore, convective heat transfer coefficient is not effected by mass flow rate. However, the mass flow rate affects the temperature rise of the circulating water. The temperature rise of the circulating water needs to be small to ensure matching the constant ambient temperature of the UCM. The mass flow rate of the water is chosen such that the temperature difference of the water at the inlet and exit of the cooling channel is approximately 1 K, which ensures constant ambient temperature boundary condition in UCM, hence the fluid temperature is taken as 300 K in the simulations of the cooling channels). Knowing the required heat flow out from UCM, the flow rate of water can be calculated using the first law of thermodynamics for the cooling channels:

$$Q = \rho \dot{V} c \Delta T \tag{2.1}$$

Taking ρ as $998\,\text{kg/m}^3$, c as $4186\,\text{J/kg}\cdot\text{K}$, ΔT is $1\,\text{K}$ as and the absorbed heat rate (Q) as $8.978\,\text{W}$ from UCM, the volumetric flow rate ($\dot{V}$) can be estimated as $128.9\,\text{mL/min}$. Several cross-sections have been assessed, and both from the thermal and fabrication point of view, and a square cross-section is selected for the cooling channels. The size of the cooling channels is selected as $2\,\text{mm} \times 2\,\text{mm}$ and the total length turns out to be approximately $0.19\,\text{m}$. For this specified cross-sectional area, the hydraulic diameter becomes $2\,\text{mm}$. Using the appropriate Nu from Figure 2.6, which is 2.98, and taking the thermal conductivity of water as $0.6\,\text{W/m}\cdot\text{K}$, the heat transfer coefficient in the cooling channels is estimated to be approximately $900\,\text{W/m}^2\cdot\text{K}$. The details of this calculations are given in the Appendix. With this cooling channel geometry and flow conditions, a heat transfer of $8.97\,\text{W}$ is achieved, which satisfies the heat removal rate boundary condition of UCM.

2.3 Design of the Heaters

In UCM, the thermal boundary condition at the evaporator section was constant wall heat flux. In the MHP system of this study, the heating will be supplied through a Cr heater located at the bottom side of the wafer. The heater geometry needs to be designed to ensure the constant wall heat flux boundary condition. The electrical field on the Cr heaters are modeled using the `Electric Current Shell Module` of COMSOL. This module enables the use of shell elements for Cr layer as 2–D plane instead of thin 3–D plate, which simplifies the meshing substantially. The electrical field on the Cr heater can be determined using the current conservation as:

$$\nabla \cdot \mathbf{J} = 0 \tag{2.2}$$

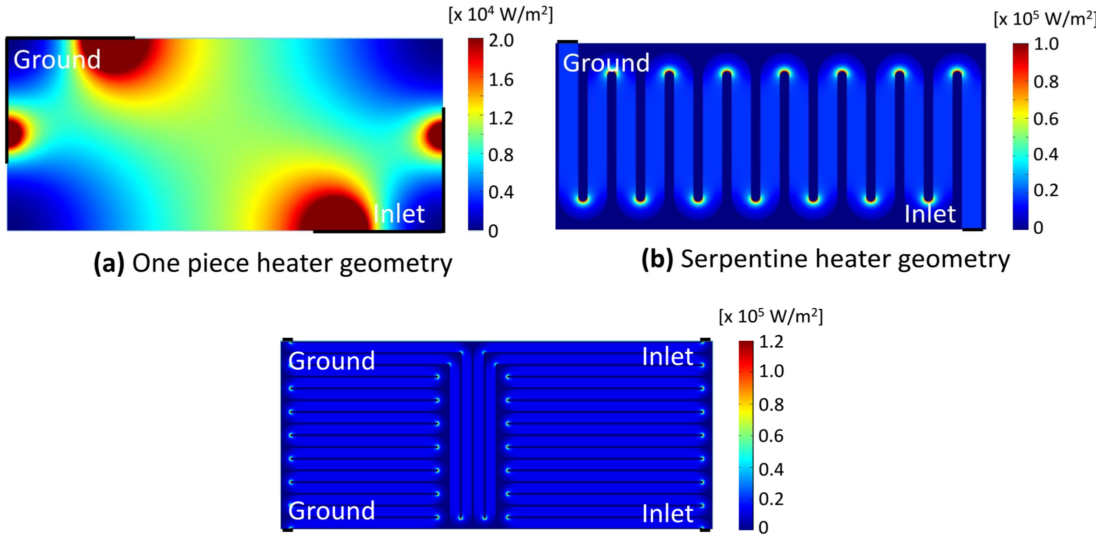

(a) One piece heater geometry

(b) Serpentine heater geometry

(c) 2 part serpentine heater geometry

Figure 2.7: The temperature distribution on the one piece, serpentine and 2 part serpentine heater geometries

where **J** is the current density. The generated heat power (Joule heating) per unit area on the Cr heater can be determined by:

$$q_{Joule} = d_s \sigma \left| \nabla_t V \right|^2 \tag{2.3}$$

where d_s is thickness of the Cr layer, σ is electrical conductivity (S/m) of the layer and ∇_t is gradient of electrical potential in tangential direction. The Joule heating power is linked to the heat transfer in solids as a highly conductive layer boundary which makes the interconnection between the two physical phenomena. The conservation of energy on the Cr coating can be written as:

$$\mathbf{n} \cdot (k \nabla T) = q_{Joule} + h(T_\infty - T) - \nabla_t \cdot (-d_s k_s \nabla_t T) \tag{2.4}$$

The first term is the heat flux through the body from the Cr thin film where $\mathbf{n}$ is the boundary normal vector and k is thermal conductivity. The third term represents convective heat flux from the Cr heater to the environment where h is heat transfer coefficient and T_∞ is the ambient temperature. The last term is heat conduction within the thin Cr layer. The thickness of the coated Cr is selected as 500 nm.

To realize the constant wall heat flux boundary condition, different heater configurations are analyzed. The simulations start with a single-piece Cr heater

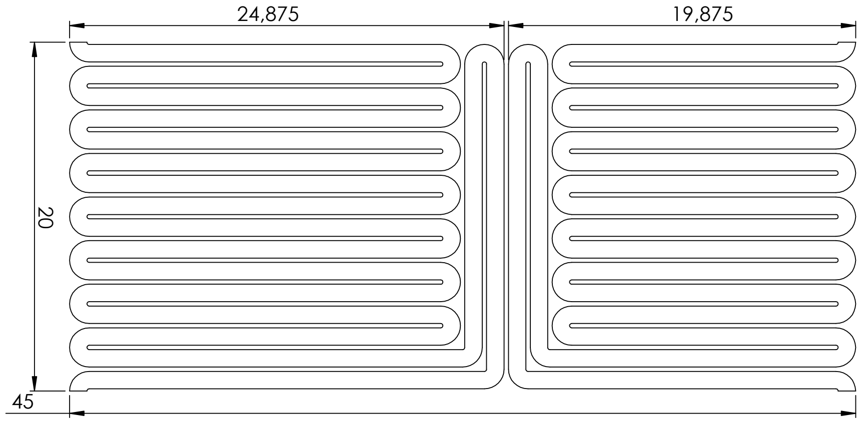

Figure 2.8: The CAD drawing of Cr serpentine heater (unit: mm)

geometry with various corner lengths as shown in Figure 2.7–(a). The result of the analysis reveals that the uniform heat flux is difficult to obtain with this geometry; therefore, a serpentine geometry is proposed. With the use of the serpentine geometry, the distribution of the heat flux becomes more uniform as presented in Figure 2.7–(b). In this case, however, there still exists a gradient. To further improve the uniformity of the heat flux, a new serpentine configuration with narrower electrodes are proposed, which is now two-piece. As shown in Figure 2.7–(c), the new configuration results in a more uniform heat flux distribution. Moreover two-piece design will give us the opportunity to set an adiabatic region when it is required in the experimentation by inactivating the applied voltage at the mid section. The final geometry of the two-piece heater can be seen in Figure 2.8. The width of the serpentine geometry is selected as 1 mm. The simulations show that a potential differences of 25.2 V and 31.7 V are needed to have the required heat flux.

2.4 3–D Multiphysics Modeling

Following the design of the cooling channels and the heater geometry, 3–D COMSOL Multiphysics simulations are conducted. The micro-grooves are placed on a standard silicon substrate which is 525 μm thick. The MHP system has cooling channels and the Cr heater at the bottom of the wafer, has micro-grooves on the top surface of the wafer, and PDMS bonder and fused silica on top of the wafer. The fused silica at the top is used to cover the middle part and house the filling holes of the working fluid for the cooling channels. The PDMS bonder is also located between the silicon wafer and the fused silica cover to form a space for the circulation of evaporated working fluid. The heat pipe micro-grooves are $200\,\mu$m $\times$ $200\,\mu$m $\times$ 75 mm in size, with a $200\,\mu$m separation between two consecutive channels, and 50 micro-grooves are present resulting in a total width of 20 mm. The simulation results in evaporator and condenser section lengths as $L_e = 45.75$ mm and $L_c = 29.25$ mm, respectively. The cooling section (PDMS cooler) is $L_{cooler} = 30$ mm in length and 20 mm in width. The Cr heater length and width are selected as $L_{heater} = 45$ mm and 20 mm.

The simulation procedure starts with the generation of the CAD model of the MHP system together with the necessary physics which are `Heat Transfer in Solids` and `Electrical Currents, Shell`. The heat transfer in the solid regions (silicon, PDMS, fused silica) is governed by the steady-state heat conduction equation:

$$\nabla \cdot (k_i \nabla T_i) = 0 \tag{2.5}$$

where k_i represents the thermal conductivity of different regions.

2.4.1 Boundary Conditions

The boundary conditions namely the heat transfer coefficients at the evaporator and condenser sections, heat removal rate from the cooler, and the electrical potential on the Cr heater are included to the relevant physics. The curve fitted data for the heat transfer coefficient along the micro-groove is applied at walls. The condenser heat flux is introduced at the top surface of the MHP micro-grooves due to the fact that the condensation of working fluid generally takes place at the top of the grooves. The evaporator heat transfer coefficient is implemented on the side walls of the MHP micro-grooves by arranging the UCM data. Because in UCM, evaporator heat transfer coefficient is applied to closer regions of the top edge - $33.33\,\mu$m, due to the fact that most of the evaporation of the working fluid occurs on the side walls. The material properties for silicon wafer, PDMS, fused silica, chromium are already defined in the simulation environment except the thermal conductivity of silicon wafer, Poisson's ratio and relative permittivity of chromium which are specified as 130, 0.21 and 1.0, respectively.

The heat transfer between the bottom surface of the fused silica (top piece of the MHP system) and the vapor of the working fluid is estimated by obtaining the appropriate Nu correlation and the heat transfer coefficient. The correlation for flow over a flat plate is used for the fused silica. The free stream velocity and temperature of the vapor is estimated based on the data in UCM. The vapor velocity and vapor temperatures are 250 mm/s and 320.7 K, respectively. The material properties of water vapor are taken from [3] for the vapor temperature. The space length L is taken as the the total length of the micro-grooves. The forced convection analysis are completed with using the following equations [3]:

$$Re = \frac{\rho V L}{\mu} \tag{2.6}$$

$$\overline{Nu}_L = \frac{\overline{h} L}{k} = 0.664 Re_L^{1/2} Pr^{1/3} \tag{2.7}$$

The Re number is calculated as 135 and the resultant heat transfer coefficient is determined as $2080\,\mathrm{W/m^2 \cdot K}$. Details of the calculation procedure, related equations, properties of vapor in the spacing, and the heat transfer coefficient are included in the Appendix.

At the outer surfaces of the MHP, natural convection heat transfer takes place. Using the Nu correlations for horizontal plate, the heat transfer coefficient for natural convection is estimated as $5\,\mathrm{W/m^2 \cdot K}$, and assigned on the outer boundary of the MHP system. The effect of the heat transfer coefficient for natural convection is also tested, and it is observed that heat transfer rate is small compared to heat transfer to the cooling water.

The applied boundary conditions on MHP system in 3–D COMSOL Multiphysics

Table 2.2: Summary of the boundary conditions used in the simulations

B.C.	Value	Description	Unit
$h_{evap.}$	curve fit	Heat transfer coefficient at evaporator	W/m^2K
$h_{cond.}$	curve fit	Heat transfer coefficient at condenser	W/m^2K
$V_{Cr,1}$	25.2	Electrical potential at Cr heater #1	Volt
$V_{Cr,2}$	31.7	Electrical potential at Cr heater #2	Volt
$d \times w$	2×2	Square pipe size of the heat sink	mm $\times$ mm
h	2080	Heat transfer coefficient on the fused silica	$W/m^2 \cdot K$
h_{cooler}	900	Heat transfer coeff. in the cooling channels	$W/m^2 \cdot K$
h_{nat}	5	Heat transfer coeff. at the outer surfaces	$W/m^2 \cdot K$
T_{cooler}	300	Inlet temperature of cooling water	K
T_∞	300	Ambient temperature	K

simulations are summarized in Table 2.2. The computational domain together with the applied boundary conditions is also presented in Figure 2.9 where the heat transfer boundary conditions on evaporator, condenser, PDMS cooler, Cr heater, spacing between the fused silica and the micro-grooves, and natural convection are marked.

2.4.2 Computation

The simulations are realized on a HP Z820 Workstation (Intel Xeon E5-2630 v2, 6 cores, 2.60GHz, 128GB RAM). In UCM, the vapor temperature was 321.8 K. When the 3–D simulation applied for this vapor temperature, it is observed that the heat transfer rates in evaporator and condenser sections are not equal and deviate from the results of UCM due to 3–D heat conduction effects within the MHP system. Additional heat conduction changes the balance of heat transfer rates at each section. At this point, one can expect that the system would reach a

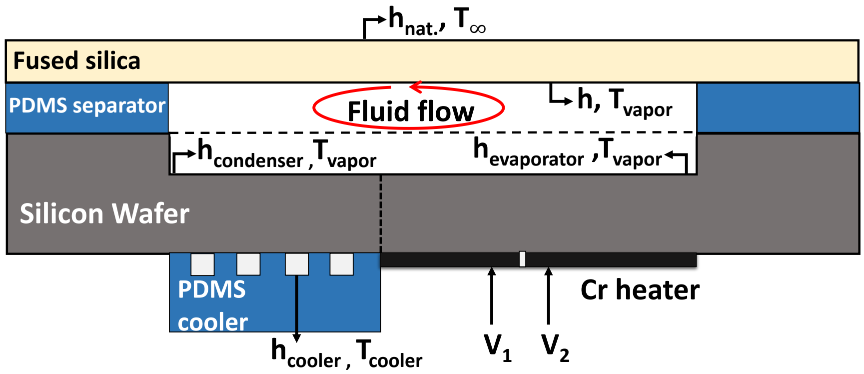

Figure 2.9: Boundary conditions of the MHP system (side view)

new equilibrium at a different vapor pressure, vapor temperature, and wall temperature. For this new equilibrium, UCM needs to be run to obtain the corrected heat transfer coefficient. However, it is expected that although heat transfer rate, the vapor temperature and the wall temperature changes, the change in the heat transfer coefficient would be comparatively small since it is known from convective heat transfer theory that heat transfer coefficient is not a strong function of temperature. Therefore, in this study, this new equilibrium condition of the MHP system is obtained by using the same heat transfer coefficients of the UCM with different vapor temperature. The closure of the equation is satisfied by checking the heat transfer rate at the condenser and the evaporator sections, which is achieved at a vapor temperature of 320.1 K in our 3–D global model. The heat transfer rates at each section for UCM and the 3–D global model is tabulated in Table 2.3. For the new vapor temperature, the transfer rates at the condenser and evaporator sections are found to be equal and 7.56 W. In addition, the 3–D model can predict the heat loss to the environment. The temperature variation on the top surface, bottom surface and at the mid-section (cut-view) can be seen in Figure 2.10. As seen from the figure, the temperatures over the microgrooves are nearly constant around 320 K. The temperature has its maximum value around the heaters.

The temperature variation at the top edge of different micro-grooves are also shown in Figure 2.11. The temperature profile along the top edge of the 1^{st}, 10^{th}, 20^{th}, 30^{th}, 40^{th} and 50^{th} MHP micro-grooves together with results of UCM are

Table 2.3: Heat transfer rate at different sections

	UCM (T_{vapor} = 321.8 K)	Global model (T_{vapor} = 320.1 K)
Q_{evap}	8.11 W	7.56 W
Q_{cond}	8.10 W	7.56 W
Q_{heater}	9.0 W	9.0 W
Q_{cooler}	8.98 W	8.38 W
Q_{loss}	——	0.62 W

presented. The difference in the temperatures is that the UCM model was well insulated; however, in 3–D global model, the effect of natural convection and heat transfer on the surface of the fused silica contact with the vapor of the working fluid are taken into account. Additionally, in the global model, the 3–D effects mainly due to the conduction heat transfer through the wafer have a significant influence on the heat transfer mechanism. The oscillations in temperatures of the condenser section are clearly seen in Figure 2.11 which are due to the serpentine geometry and the separation between each turn (which is 1 mm) of the cooling channels. However, the temperature change is not critical and serpentine channels are a more suitable way to transfer heat uniformly from the cooler section. In temperature profiles on the MHP micro-grooves, except for the 1^{st} and 50^{th} micro-grooves located at the two ends, the wall temperatures show the same trend as seen in the temperature profile in the 10^{th}, 20^{th}, 30^{th} and 40^{th} micro-grooves. 1^{st} and 50^{th} micro-groove temperatures show slightly different variations especially in the evaporator region due to heat transfer from Cr heater to Si wafer. These effects originate from the 3–D geometry which cannot be predicted by UCM. In specified locations, the heater geometry is changed to reduce the space between Cr coatings of the heaters which ensures a uniform Joule heating.

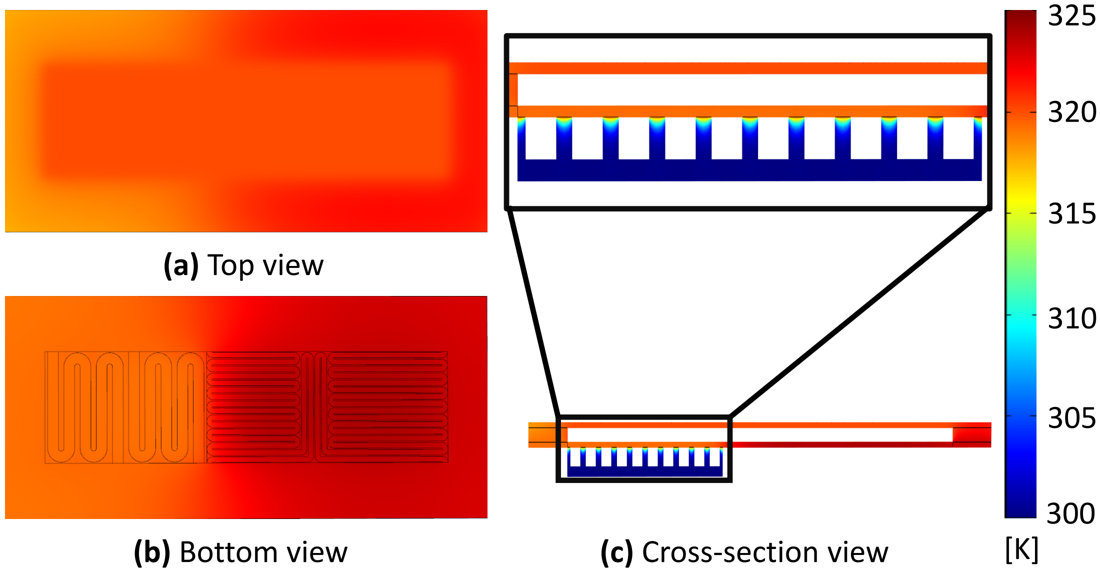

Figure 2.10: The temperature distribution of the MHP system

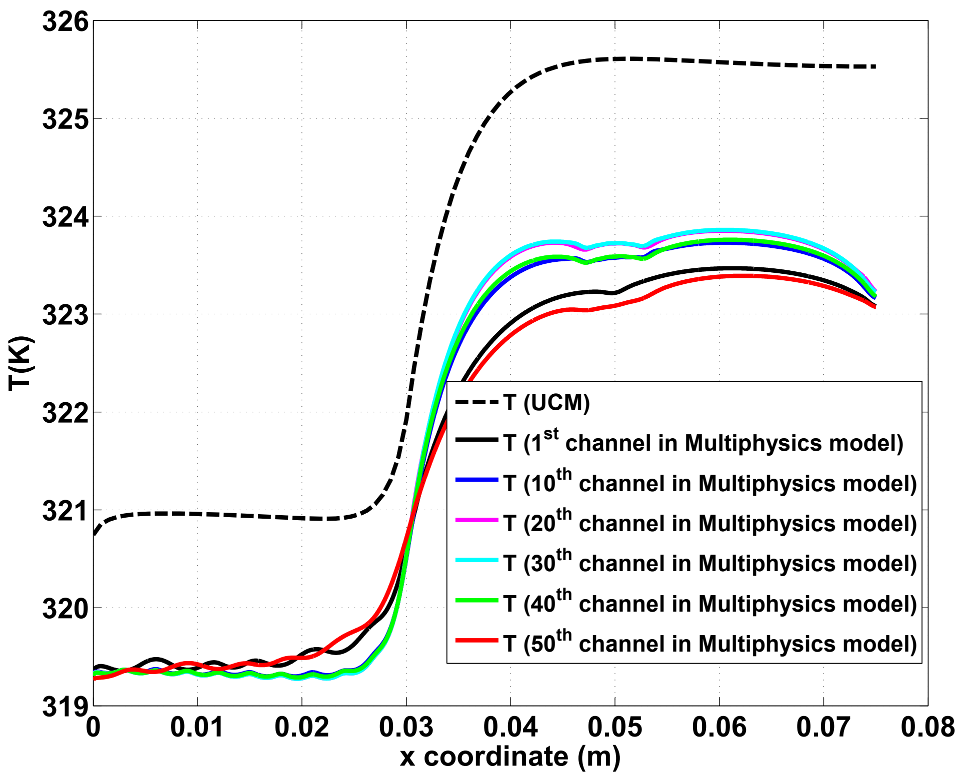

Figure 2.11: The temperature distributions along the micro-grooves

2.5 Mesh Optimization and Independence

Considering that the length scale of the geometries range from nm (thickness of the deposited Cr) to cm (overall dimensions of the wafer) levels, the meshing becomes critical to reach appropriate results with an acceptable computational power and time. A proper meshing of all these length scales requires a prohibitively large number of mesh elements at an extreme computational cost. Moreover, large number of degrees of freedom (DOF) may create convergence problems. Therefore, meshing of the MHP system is studied extensively in this work.

To eliminate the meshing problems regarding the nm−scale electrode thickness, the shell module of the COMSOL is used which models the electrical field in 2–D. The next critical step of the meshing is the meshing of the micro-grooves. These micro-grooves have a high length-over-diameter (i.e. hydraulic diameter) ratio (which is 375). Moreover, there are 50 micro-grooves, in addition the overall dimensions are in the order of cm's. In this thesis, it is observed that with meshing without any optimization, the overall system will have around 50M DOF, which makes it impossible to solve with the available computational power. Moreover, even though 50M DOF becomes solvable, the solution time would be very long which would make the computation unfeasible. All these issues make the mesh independence also challenging. Therefore, a mesh optimization is performed for each sub-computation (i.e. modeling of unit cell, modeling of cooling channels and modeling of heaters), and the mesh independent sizes are used in the 3–D global model.

The first mesh optimization analysis is performed for the unit cell computations. There is an important detail about the unit cell modeling that is in UCM, the evaporation is included at the top portion of the micro-groove (a region with 33 μm thickness), since the majority of the evaporation takes places at this region [11]. However, to mimic that behavior, a very small mesh size needs to be used. To avoid this, in our model the same amount of heat transfer is distributed over the entire side wall. Two-sets of mesh configurations with tetrahedral mesh elements

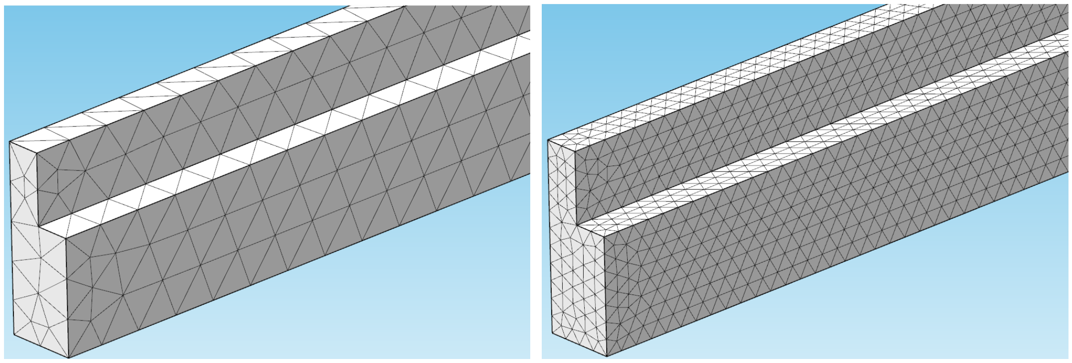

(a) (b)

Figure 2.12: Mesh elements used for modeling of unit cell: **(a)** Coarse mesh (62k DOF), **(b)** Fine mesh (1.1M DOF)

are used as seen in Figure 2.12. The coarse mesh includes only two meshes in the vertical direction on the side-wall of the micro-groove and the fine mesh includes five mesh on the side-wall. However, 2.5 times more mesh in the height direction results in almost 20 times more DOF (coarse mesh has 62,000 DOF, fine mesh has 1,100,000 DOF). For the coarse mesh configuration maximum element size, minimum element size and the growth rate is arranged to 125 μm, 25 μm and 1.5 respectively. For the fine mesh configuration, the same parameters are appointed to 50 μm, 15 μm and 1.5. For these two-set of mesh configurations, COMSOL simulations are performed and compared with the results of UCM as shown in Figure 2.13. As seen from the figure, the results of the coarse mesh and fine mesh are indistinguishable. Therefore, in the 3–D global modeling, coarse mesh configuration of the unit cell modeling is used.

The second mesh optimization analysis is performed for the cooling channels. Three-sets of mesh configurations with tetrahedral mesh elements are analyzed as seen in Figure 2.14. As seen from the figure, finer mesh elements are used at the top wall of the cooling channels due to the compatibility with the mesh elements on the micro-grooves. For the all mesh configurations, the element growth rate is set to 1.5. For the coarse mesh configuration, maximum element size and minimum element size are adjusted to 1 mm and 100 μm, respectively. For the interior surface of the channels, a different set of mesh parameters are defined and they have maximum element sizes of 500 μm and minimum element sizes of

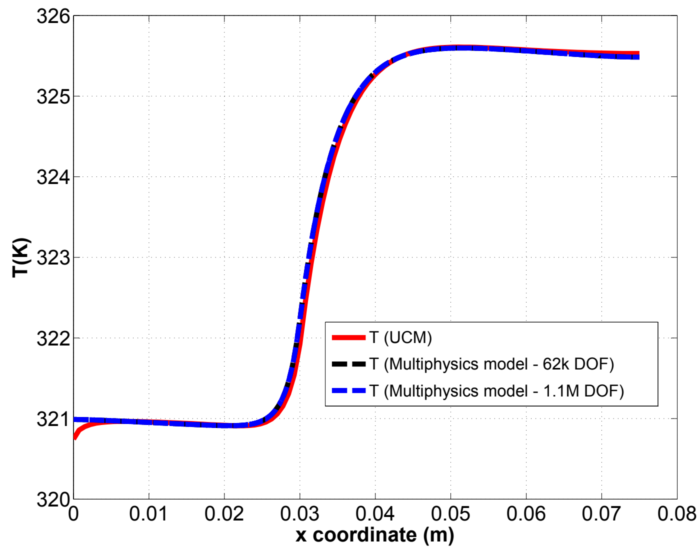

Figure 2.13: Comparison of different mesh configurations for the unit cell

100 μm. The total number of DOF becomes 280,000 for the coarse mesh configuration. For the fine mesh configuration, the maximum element sizes for the subdomain and for the interior surfaces are defined as 500 μm and 125 μm, respectively. The minimum element size of the subdomain and the interior surfaces are arranged as 15 μm. The total number of DOF becomes 2,000,000 for the fine mesh configuration. For the finer mesh configuration, the maximum element sizes for the subdomain and for the interior surfaces are set to 500 μm and 75 μm, respectively. The minimum element size of the subdomain and the interior surfaces are set to 15 μm. The total number of DOF becomes 5,500,000 for the fine mesh configuration.

The temperature variation on the top surface of the cooling channels (at the mid-section in the horizontal direction of the MHP system) has been compared for different mesh configurations and presented in Figure 2.15 in which temperatures match except for the intersection of silicon, cooling channels and the PDMS. From this analysis, the fine mesh configurations (i.e. case with 2M DOF) is selected to be used in the 3–D global model.

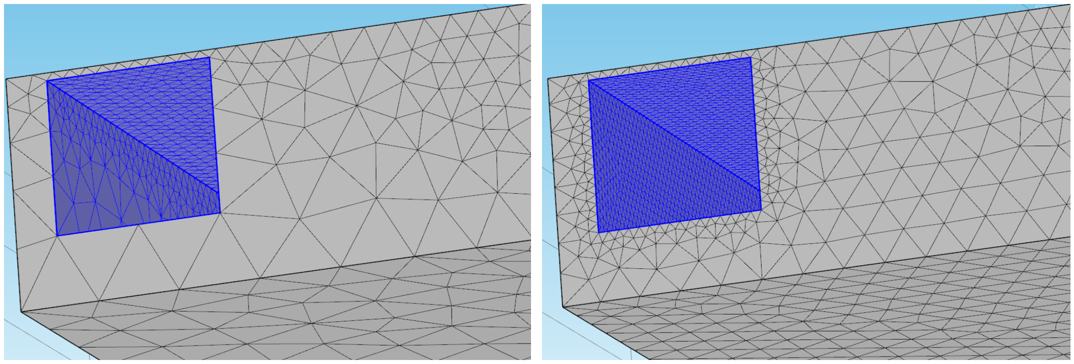

(a) (b)

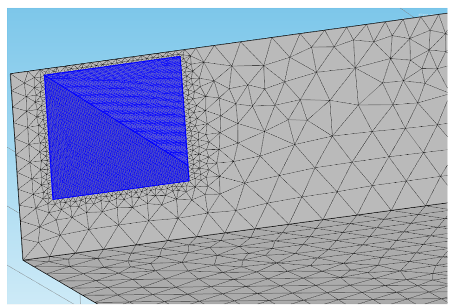

(c)

Figure 2.14: Mesh elements used for modeling of the cooling channels: **(a)** Coarse mesh (280k DOF), **(b)** Fine mesh (2M DOF), **(b)** Finer mesh (5.5M DOF)

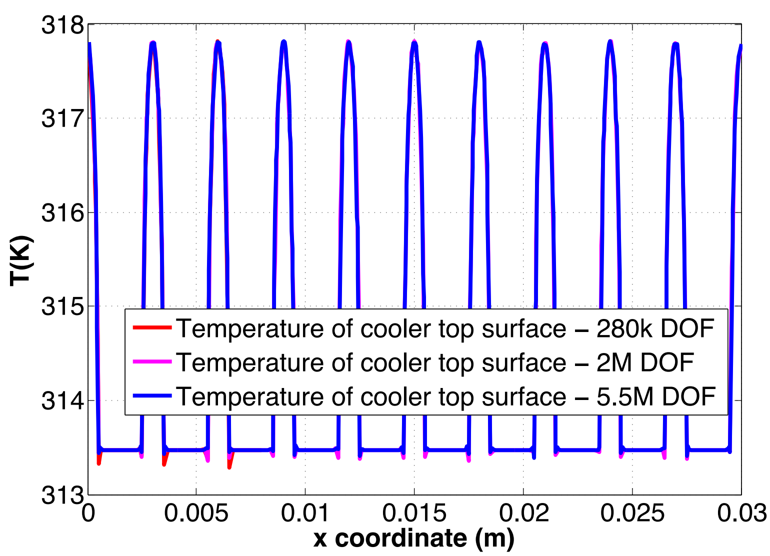

Figure 2.15: Comparison of different mesh configurations for the cooling channels

The third mesh optimization analysis is performed for the Cr heater. Mesh element size is critical for Cr heater geometry due to the curved shape; therefore, a finer element size is required and selected accordingly. Three-sets of mesh configurations with tetrahedral mesh elements are analyzed andshown in Figure 2.16. For all mesh configurations, the element growth rate is set to 1.5. For coarse mesh configuration, the maximum and minimum element sizes are set to 1 mm and 100 μm, respectively. On the surface of the Cr heater, a different set of mesh parameters are defined. The maximum and minimum element sizes used are 500 μm and 100 μm, respectively. The total number of DOF becomes 550,000 for the coarse mesh configuration. For the fine mesh configuration, the maximum element sizes for the subdomain and for surface of the heater are assigned to 1 mm and 100 μm, respectively. The minimum element size of the subdomain and the Cr heater are set to 50 μm. The total number of DOF becomes 2,200,000 for the fine mesh configuration. For the finer mesh configuration, the maximum element sizes for the subdomain and for the Cr heater geometry are applied as 500 μm and 25 μm, respectively. The minimum element size of the subdomain and the interior surfaces are set to 15 μm. The total number of DOF becomes 6,500,000 for the fine mesh configuration. For mesh independence, the temperature variation along the Cr heater surface (at the mid-section in the horizontal direction of the MHP system) is represented. It is clearly seen that the temperature variations match perfectly for all cases. However, to obtain a smooth transition at the curved regions, the fine mesh configuration (i.e. case with 2.2M DOF) is selected to be used in the 3–D global model.

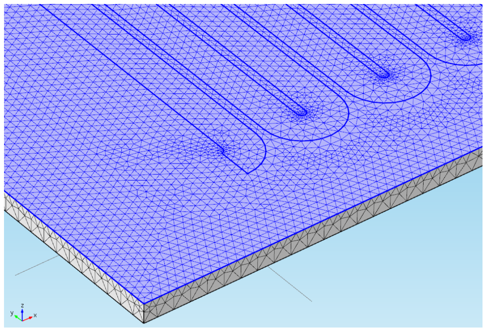

(a)

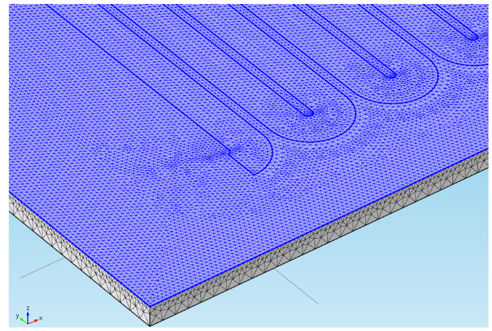

(b)

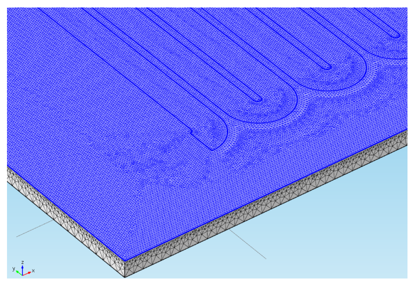

(c)

Figure 2.16: Mesh elements used for modeling of the Cr heater: **(a)** Coarse mesh (550k DOF), **(b)** Fine mesh (2.2M DOF), **(b)** Finer mesh (6.5M DOF)

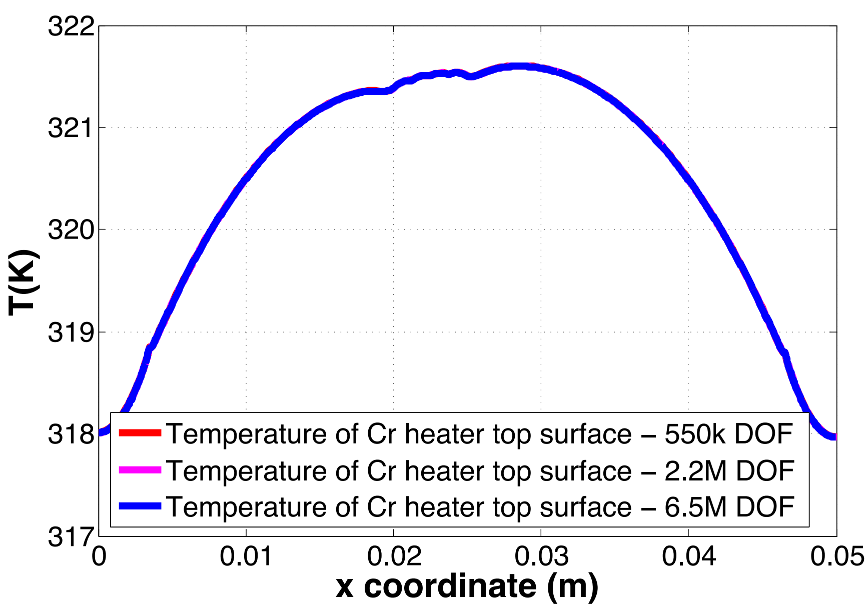

Figure 2.17: Comparison of different mesh configurations for the Cr heater

In the light of the mesh optimization and independence study, the mesh of the MHP system is generated using the aforementioned mesh parameters. The meshing of the MHP system can be seen in Figure 2.18. A total number of 12.5M DOF is obtained for the demonstrated mesh configuration. A typical run with this c-mesh configuration takes approximately 15 minutes of CPU time with a 30 GB of physical memory usage.

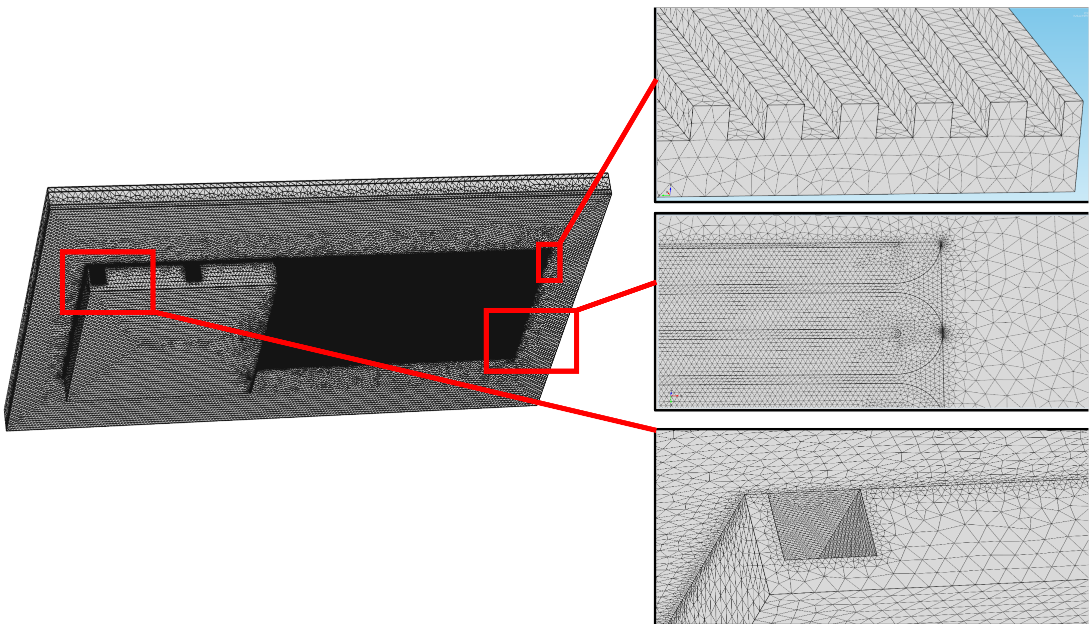

Figure 2.18: Mesh of the MHP system

Chapter 3

Fabrication of the MHP System

Fabrication of Si micro-groove heat pipe has several steps, namely: **(i)** fabrication of the micro-grooves, **(ii)** fabrication of the cooling channels, **(iii)** fabrication of the Cr heater, and **(iv)** assembly of the system. The fabrication of the micro-grooves is performed by two main techniques namely lithography-based and mechanical-based. In lithography-based fabrication, photoresist is used as a protective layer and etching process is applied to obtain anisotropic micro-groove walls. In mechanical fabrication, cutting with an automated diamond saw and high-precision machining with a diamond tool and a PCB tool are used. The lithography-based fabrication and the dicing saw techniques are performed at the Bilkent University National Nanotechnology Research Center, and high-precision machining is performed at the Bilkent University Micro System and Design Center. The cooling channels are fabricated using PDMS molding technique. The mold of the cooling channels is fabricated using high-precision mechanical machining. The fabrication of the Cr heaters is performed using micro-fabrication techniques in the cleanroom environment. At the final step, all the pieces are assembled. Following the fabrication processes, the groove profiles are inspected using a scanning electron microscope (SEM) and a 3D Laser Scanning Confocal Microscope (VK-X100, KEYENCE Corporation). Details of the fabrication procedures and process parameters are explained in the upcoming sections.

3.1 Fabrication of the Micro-grooves

3.1.1 Lithography-based Fabrication

Lithography-based fabrication has been accomplished with plasma (dry) etching process. In plasma etching, the etchant chemicals are in gases form [43] and used to chemically etch substrate to open grooves. This fabrication technique consists of two main steps which are photolithography and dry etching. These steps are briefly explained and prepared recipes of photolithography and dry etching for the micro-groove fabrication are given below. The lithography-based fabrication of this thesis work has been performed using the facilities of Bilkent University National Nanotechnology Research Center.

3.1.1.1 Photolithography

Photolithography is most widely chosen lithography technique and commonly used in IC fabrication due to complex and high-aspect ratio feature preparation capabilities [44]. Additionally, this technique is very convenient for mass production such that when the necessary recipes are optimized, many samples can be processed at the same time with less effort. Main elements of photolithography are a UV light, photomask and photosensitive material (photoresist). Common steps of photolithography can be divided into four which are film deposition, spin coating, exposure and development. For the sake of the simplicity, schematic of these steps is shown in Figure 3.1, and details of these steps are explained below [45]:

1. **Film deposition:** According to requirements of this fabrication process, a film in the form of metal, silicon oxide, silicon nitride, polymers, etc. is patterned on the substrate with deposition. General film deposition techniques are spin coating, sputtering, evaporation, and oxidation.

2. **Spin coating:** Photoresist (photo sensitive polymer) is coated uniformly

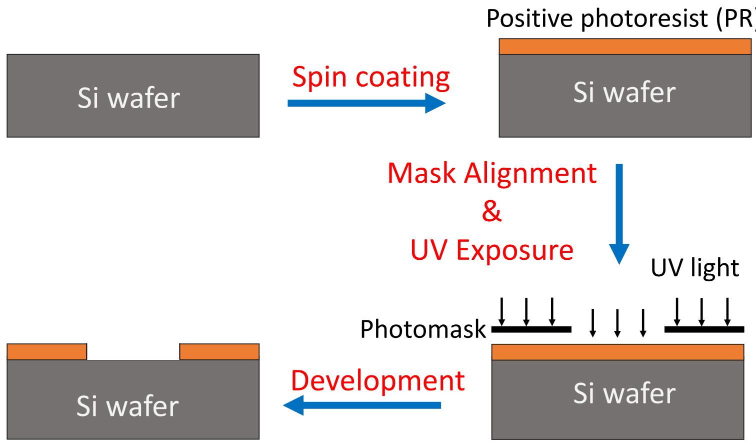

Figure 3.1: Schematic of a photolithography process

on the wafer by the centrifugal force effect with spin coater. Thickness of the photoresist can be adjusted with tuning the rotational speed of the spin coater. Typically, maximum possible coating thickness of photoresist according to rotational speed is given by manufacturer. Moreover, the photoresist needs to cover the substrate surface uniformly which ensures the conformity of the lithography. Following the coating of the photoresist, soft bake is applied between 90-100℃ to release the solvent inside the photoresist.

3. **Exposure:** Photoresist coated substrate is exposed to UV light to pattern desired geometries on the substrate by using photomask. Photomask can be a special glass, an acetate or a silica plate with metal cover which is generally electron-beam lithography coated chromium film layer. The necessary geometries need to be patterned on the photomask and if precise alignment is needed, alignment marks needs to be placed on the photomask.

4. **Development:** Lift-off unwanted regions of the photoresist is performed using developing solutions or spray developer. Developing solution is usually a mixture of special chemicals called as developer and DI water. Positive and negative photoresist are two types of photoresists. Depending on the

photoresist types, UV light exposed surfaces behaves differently. In positive photoresist, the exposed area becomes solvable, however for negative photoresist, unexposed area becomes solvable. Development process continues with the hard baking process at 120-180℃ which helps to strengthen the photoresist structure and enhance bonding of the photoresist to the substrate.

Photolithography recipe for the sample preparation of a silicon wafer for DRIE process can be listed s follows:

(1) Cleaning: Clean Si wafer with acetone, isopropanol and DI water and then placing the sample on hot plate for 5 min to dry-out the residual water.

(2) Spin Coating: Coat HMDS and AZ 4562 photoresist with spin coater: **(i)** HMDS at 4000 rpm for 40 seconds with an angular acceleration of 1088 rpm/s , **(ii)** AZ 4562 photoresist at 2000 rpm for 30 seconds with an angular acceleration of 408 rpm/s.

(3) Soft Bake: Bake sample in room temperature for 5 min., and on hot plate for 1.5 min. at 110℃ to improve bonding of photoresist to sample. Cool the sample for 5 minutes at room temperature.

(4) Exposure: 400 mJ/cm^2 dose of UV light exposure with using EVG 620 Automated Mask Alignment System .

(5) Development: Develop the sample about 5 minutes (developing solution contains AZ 400K developer from MicroChemicals and DI water with the volume ratio of 1:4).

(6) Hard Bake: Hard bake the sample for 15 minutes at 90℃ on hot plate. Then cool the sample at room temperature for 10 minutes.

3.1.1.2 Plasma (Dry) Etching

Plasma (Dry) etching is a physical and chemical process for material removal from substrates. It is preferred due to the ability of anisotropic etching which generates vertical wall profiles [46]. Therefore, this process has been selected to fabricate micro-grooves on silicon wafer in which sharpness of micro-groove edges are crucial for capillary pressure constitution which is the driving force for liquid from condenser to evaporator region. Deep Reactive Ion Etching (DRIE) is a type of plasma etching used to fabricate high aspect ratio structures such as nearly perfect side walls with depth of hundreds of microns [43]. It is generally used for the etching of silicon. This technique was first invented by Robert Bosch GmbH this is the reason the process is mostly called as Bosch process. Etching and deposition are two main steps in Bosch process [45]. These steps can be described as following:

- **Etching**: It is standard process of plasma etching. Etching process conducted with SF_6 as a reactive gases. Fluorine plasma (F^+) etches the sample where it has direct contact with surfaces mainly in vertical direction [46].
- **Deposition (Passivation)**: In this step, C_4F_8 or CHF_3 gases helps to deposited fluoropolymer passivation layer on sample to avoid lateral etching [46].

The schematic of the basic steps of DRIE cycle (etching-deposition) can be seen in Figure 3.2

DRIE process differs from Reactive Ion Etching (RIE) in terms of etch rate, selectivity, aspect ratio capability or reactor type. In DRIE, there are generally two RF power generator placed in the system and inductively coupled plasma (ICP) source used to create high-density plasma that increases the etch rate about 1-2 order of magnitude compare to RIE [46]. Due to the etching technique which consists of physical and chemical operations, the process is very complex

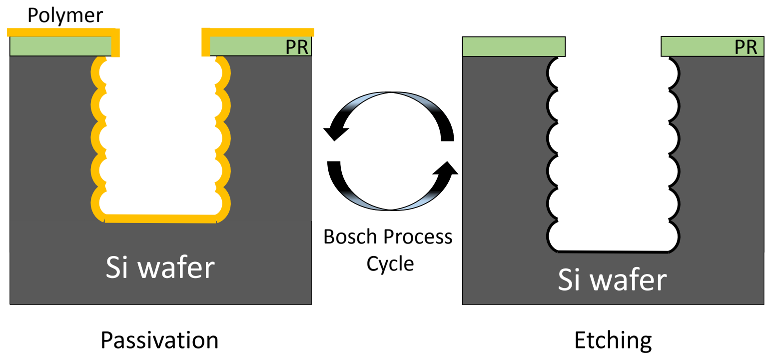

Figure 3.2: Schematic of basic DRIE process cycle

Table 3.1: Effects of DRIE process parameters (Adapted from [4])

Increasing Paramaters	**Etch Rate**	**Wall Profile**	**Selectivity**
SF_6 Flow	Increases	Negative	Increases
C_4F_8 Flow	Decreases	No effect	Increases
Etch: Dep. time ratio	Increases	Negative	Increases
Pressure	Increases	Negative	Increases
Platen Power	Increases	Negative	Decreases
Coil Power in Etch	Increases	Negative	Increases
Coil Power in Deposition	Decreases	Positive	Increases

and many parameters need to be adjusted and optimized [43]. These parameters can be listed as: etchant gases, flow rate of the chosen gases, RF-power (coil power in ICP), bias voltage (Capacitively coupled plasma (CCP) power in ICP), process pressure and temperature [46]. The effects of these parameters on etch rate, wall profile and selectivity are tabulated in Table 3.1. From Table 3.1, it can be concluded that the etch rate of sample decreases with the increase of C_4F_8 flow and deposition coil power which increases the passivation as a result polymer layer thickness and consequently, lowers the etching. The groove profile shows negative wall angle that is undercut of the sample under the photoresist for all the parameters except C_4F_8 flow and deposition coil power. This is due to the increase of the fluorine plasma on the camber which increases the etching. Passivation gas (C_4F_8) flow shows no considerable change in the channel profile

Table 3.2: Selected DRIE process parameters (Base Recipe)

	Passivation	**Etching**
Cycle time	7 s	10 s
Pressure	18 mT	35 mT
C_4F_8 flow	70 sccm	-
SF_6 flow	-	80 sccm
O_2 flow	-	5 sccm
Ar flow	-	-
Coil Power	400 W	400 W
Bias Power	-	13 W
Bias Frequency	-	13.56 MHz
Platen Chiller	20^oC	20^oC
Lid Heater	-	45^oC
Platen matching (Full Auto)	Load 35, Tune 50	Load 35, Tune 50
Coil matching (Full Auto)	Load 37, Tune 50	Load 37, Tune 45

whereas the increase in the coil power deposition decreases the etching from the close region to the photoresist edges which creates trapezoid groove shape with positive channel wall profile. Selectivity of photoresist and substrate play important role in etching ,and it decreases with the increase of the platen power which is mainly because of the increase in the energy of fluorine plasma (F^+) which etches both photoresist and substrate.

DRIE process has been conducted on the photolithography applied samples and tested for the DRIE recipe which can be viewed in Table 3.2. Several trials has been completed for different sample configurations and recipe parameters. For each cases, the reflectivity parameters on micro-groove geometry are investigated and important conclusions have been deduced. These conclusions can be summarized as follows:

- **Sample size and configuration:** The available DRIE facility in National

Nanotechnology Research Center has sample holder which is suitable for 4'' wafers (which will be called as full-wafer hereafter). Therefore, the smaller size samples can be placed on a dummy wafer (work as a carrier wafer which is selected as soda lime). The cooling of the sample while Bosch process is directly related with the sample size. Small samples has less heat transfer surfaces which leads to diminish of the effects of passivation and etching gases.

- **Substrate Temperature:** Substrate temperature is crucial during the Bosch process since the effective cooling of the sample increases the performance of passivation and etching. DRIE process has been applied on three sample configurations which are small samples (25 mm × 25 mm) placed on carrier wafer, small samples bonded to carrier wafer and full-wafer. The bonding of the samples on carrier wafer which selected as 4'' soda lime has been achieved with using AZ 5214 E photoresist. Bonding operation of small samples starts with the spin coating of a photoresist on a soda lime. It can be mentioned that thinner the photoresist thickness, much better the heat transfer between sample and carrier wafer because of the decrease in the thermal resistivity between the sample and the carrier wafer. Nevertheless, the thickness of photoresist needs to be enough to bond the sample with the carrier wafer. Applied parameters for bonding operations can be listed as: **(i)** Spin coating of AZ 5214 E photoresist (2000 rpm for 30 seconds with an angular acceleration of 408 rpm/s) on soda lime, and **(ii)** baking of the sample for 25 minutes at 100°C. Additionally, a force needs to be applied at the corners of sample to evacuate trapped air between sample and soda lime (carrier wafer).

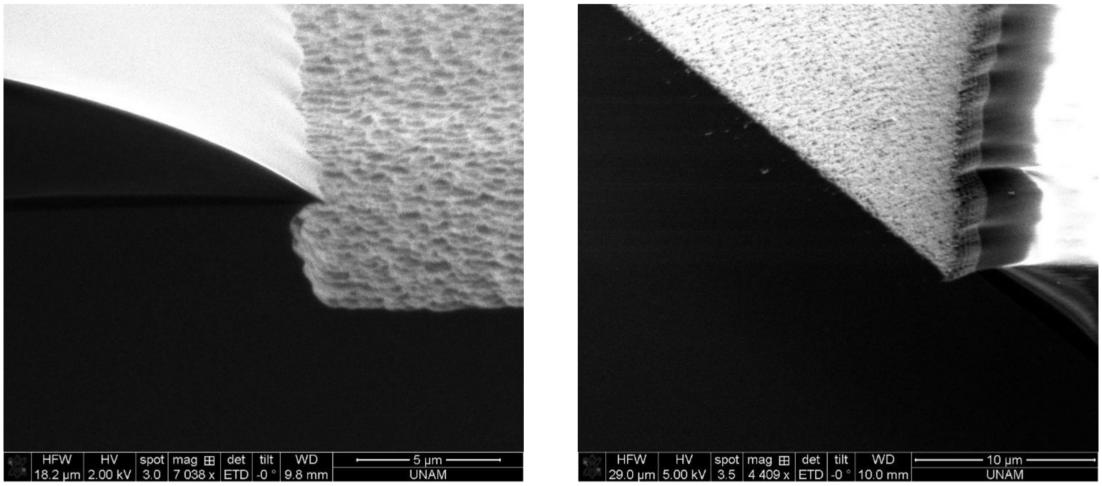

(a) 10 cycles DRIE process on sample without bonded to carrier wafer

(b) 10 cycles DRIE process on sample bonded to carrier wafer

Figure 3.3: SEM images of micro-grooves for 10-cycles on small samples

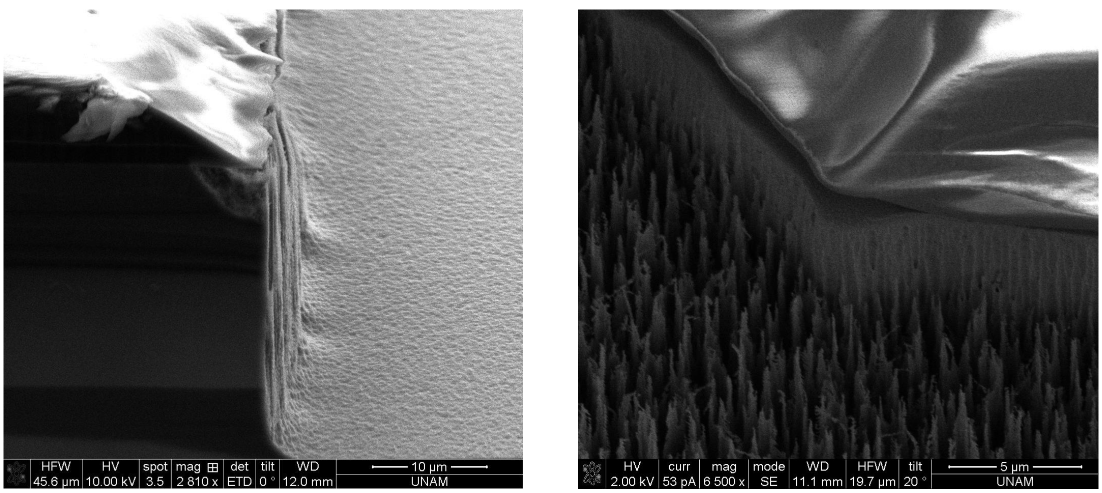

(a) 50 cycles DRIE process on sample bonded to carrier wafer

(b) 50 cycles DRIE process on full wafer

Figure 3.4: SEM images of micro-grooves for 50-cycles

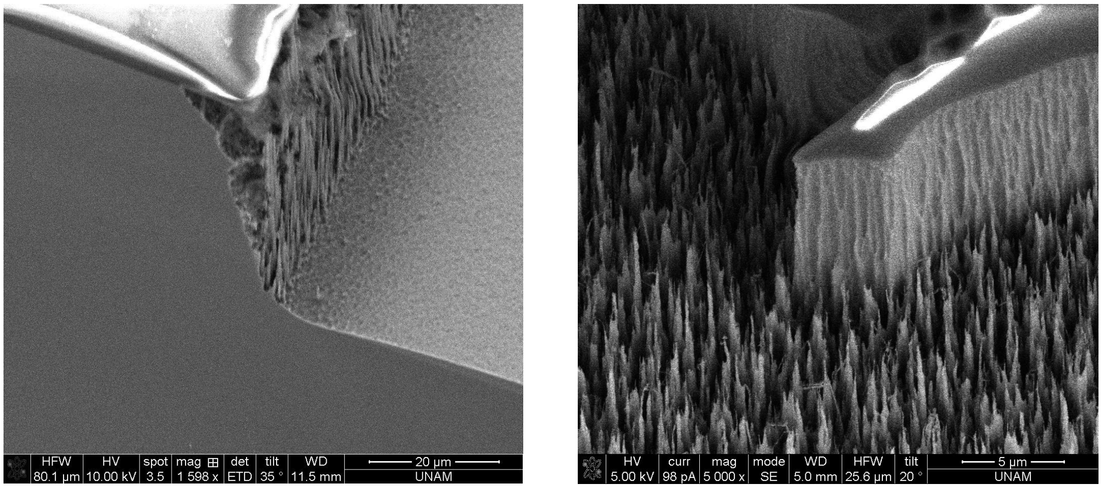

(a) 100 cycles DRIE process on sample bonded to carrier wafer

(b) 100 cycles DRIE process on full wafer

Figure 3.5: SEM images of Si micro-grooves for 100-cycles

Trials on small samples with and without bonding to soda lime reveal that an improper cooling of the sample negatively effects the etching, and the photoresist on the sample melts especially at the thinner locations. Moreover, undercut is observed under the photoresist. Figure 3.3 shows the micro-groove profiles for 10-cycles of Bosch process with base recipe on small samples which are placed on s soda lime with and without bonding where the photoresist can be easily distinguished from the wafer. It can be concluded that bonding of the sample to a carrier wafer increases the heat transfer on the sample as a result, effectively cools the sample and in parallel with that low temperature slows down the chemical reaction that produces isotropic etching. Additionally, scallops has been obtained as seen in Figure 3.3–(b), due to improvements in sidewall passivation [4]. Moreover, temperature effects on the micro-groove profiles for the sample bonded on a soda lime and full-wafer has been tested for 50- and 100-cycles of base recipe as shown in Figure 3.4 and 3.5. Unlike the previous attempts, cooling is further improved on full-wafer. As a result, too much passivation is observed which causes grassing at the bottom of micro grooves as shown in Figure 3.4–(b) and 3.5–(b). Addition to that, in Bosch process on the bonded sample, undercut has been observed underneath the photoresist,

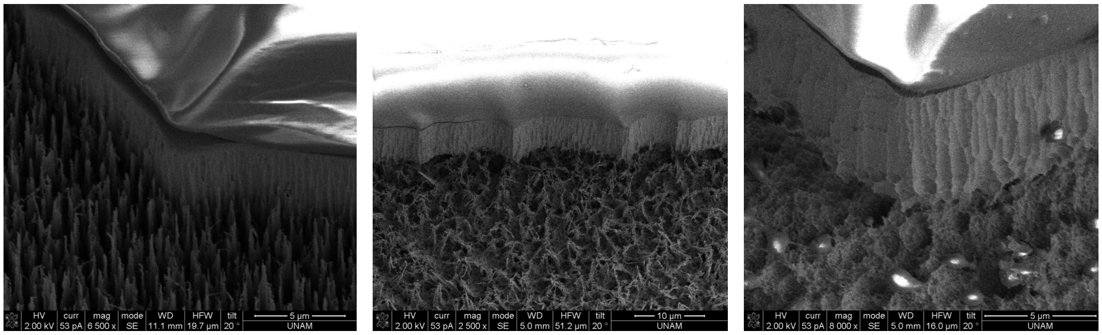

(a) 50 cycles DRIE process on full wafer C_4F_8 flow rate of 70 sccm **(b)** 50 cycles DRIE process on full wafer C_4F_8 flow rate of 50 sccm **(c)** 50 cycles DRIE process on full wafer C_4F_8 flow rate of 40 sccm

Figure 3.6: SEM images of micro-grooves for 50-cycles

however a satisfactory perpendicularity of the side-walls is achieved, and no grassing has been observed. Increasing cycle number from 50 to 100, undercut has grown and the side-walls of the grooves becomes non-vertical. Moreover, scallops become more dominant on side-walls whereas no grassing is observed as seen in Figure 3.5–(a)

Undercut and grassing (if it is above 5% of the height of the micro-groove) formations are not desired features for the micro-grooves of the MHP. Therefore, reducing the passivation components by adjusting the flow rate or increasing the platen power are two ways to overcome grassing and undercut problem [4]. On this basis, the next attempts are focused on the reduction of grasses with decrease in flow rate of C_4F_8 for a 50-cycles of Bosch process with full-wafer. The results are shown in Figure 3.6. Figure 3.6–(a) shows the result of the same recipe with a C_4F_8 flow rate of 70 sccm. Figure 3.6–(b) shows the case with a flow rate of 50 sccm. As depicted from the figures, the grassing is reduced with the reduces flow rate, however crater-like formations are formed. Further decrease in the flow rate from 50 sccm to 40 sccm, the crater-like formations are more pronounced. The resultant micro-groove surface profile has been represented in Figure 3.6–(c). It is observed that the crater-like structures diminishes the etching in the vertical directions and results in undercut beneath the vertical side-walls.

- **Effect of passivation gas flow rate and passivation deposition time:** In this trials, all samples are bonded to a soda lime and the base recipe (3.2)

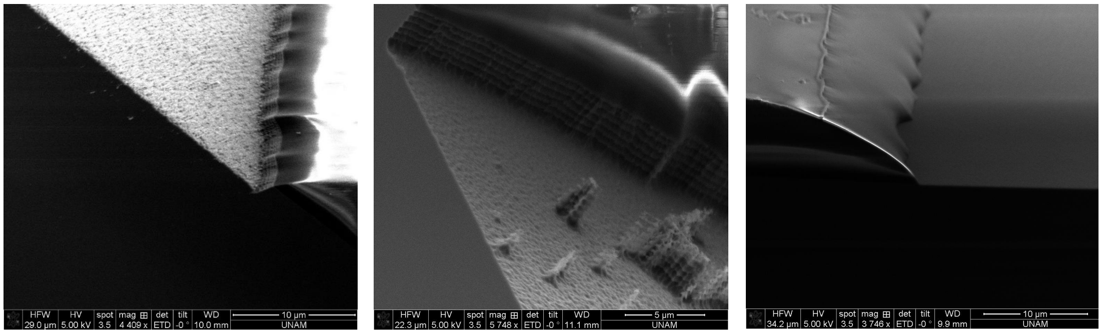

(a) 10 cycles DRIE process on sample bonded to carrier wafer with C_4F_8 flow rate of 70 sccm and passivation deposition time of 7 sec (base recipe)

(b) 10 cycles DRIE process on sample bonded to carrier wafer with C_4F_8 flow rate of 100 sccm

(c) 10 cycles DRIE process on sample bonded to carrier wafer with passivation deposition time of10 sec

Figure 3.7: SEM images of Si micro-grooves for 100-cycles

is applied except the passivation gas flow rate and passivation deposition time has changed in the second and third trials. The resultant etching profiles can be seen in Figure 3.7. The flow rate of passivation gas changed from 70 sccm (base recipe) to 100 sccm, and micro-groove profiles shown in Figure 3.7–(b) are achieved. When the micro-groove profiles are compared, the scallops can be seen clearly, and the major difference is the grassing formation in base recipe whereas there is no grassing for the case in which the passivation flow rate increases. Perfectly vertical walls with trenches has been observed with these recipes. The depth of etchings are measured as $3.3\,\mu$m to $3.5\,\mu$m. In the case of increased passivation time from 7 sec to 10 sec, a thicker layer of C_4F_8 is formed which deteriorates the etching. Therefore, in Figure 3.7–(c), there is no etching observed and the change in the form of the photoresist at the edges are clearly seen.

By considering all tested parameters, a final recipe is prepared and tested on a full-wafer. The desired depth of micro-groove (200 μm) has been obtained for 580 cycle with grassing. No undercut and photoresist deformation has been observed with this final recipe. The SEM images of micro-groove profiles and the full MHP micro-grooves can be seen in Figure 3.8.

Table 3.3: Selected DRIE process parameters (Final Recipe)

	Passivation	**Etching**
Cycle time	7 s	10 s
Pressure	20 mT	35 mT
C_4F_8 flow	70 sccm	-
SF_6 flow	-	80 sccm
O_2 flow	-	5 sccm
Ar flow	-	-
Coil Power	400 W	400 W
Bias Power	-	13 W
Bias Frequency	-	13.56 MHz
Platen Chiller	20^{o}C	20^{o}C
Lid Heater	-	45^{o}C
Platen matching (Manual)	Load 35, Tune 50	Load 35, Tune 50
Coil matching (Full Auto)	Load 40, Tune 60	Load 40, Tune 50

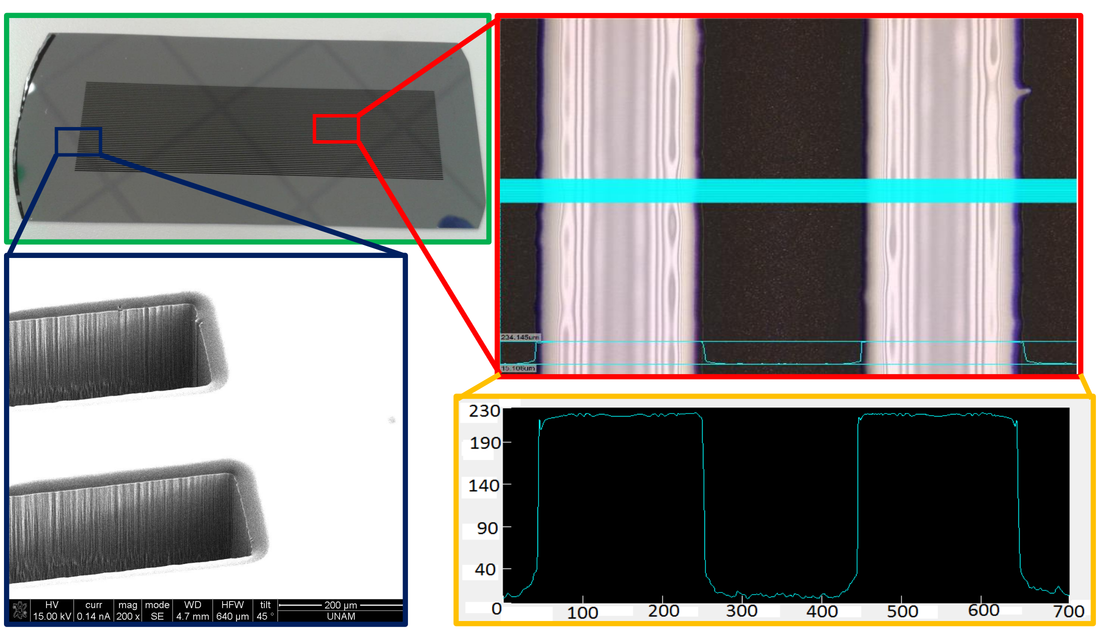

Figure 3.8: Microscopic image and profiles of micro-grooves (unit: μm)

3.1.2 Mechanical Fabrication

As an alternative to lithography-based fabrication, two different mechanical fabrication techniques namely cutting with automatic dicing saw and high precision mechanical machining are assessed for the fabrication of the micro-grooves.

3.1.2.1 Automatic Dicing Saw

Micro-grooves is fabricated on Si wafer with automatic dicing saw (Disco DAD3220 - equipment of National Nanotechnology Research Center) which has a diamond saw with a diameter of 50 mm. Initially, micro-grooves fabricated on a Si wafer from the edge of the wafer by chip removing from one side to other side for 200 μm depth. During this process, away from the wafer, the dicing blade moves in the vertical direction with one step (200 μm) from level of top surface of the Si wafer. The dicing blade rotates with the speed of 30000 rpm and chip removal started with horizontal movement of the blade. Vertical side-walls with a perfect channel profile and nm level surface roughness is achieved without any chip removal from the channel edges (see Figure 3.9–(a)).

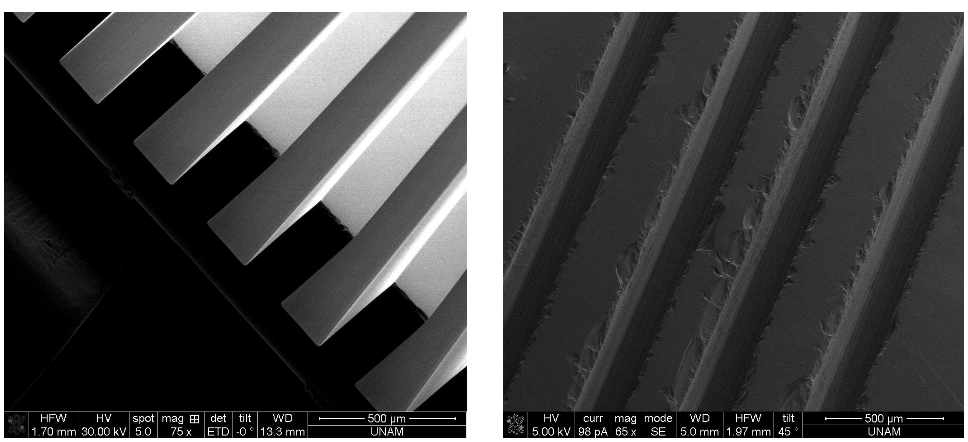

(a) Open ended micro-grooves

(b) 50 µm step depth of cut applied micro-grooves

Figure 3.9: SEM images of micro-grooves fabricated by automatic dicing saw

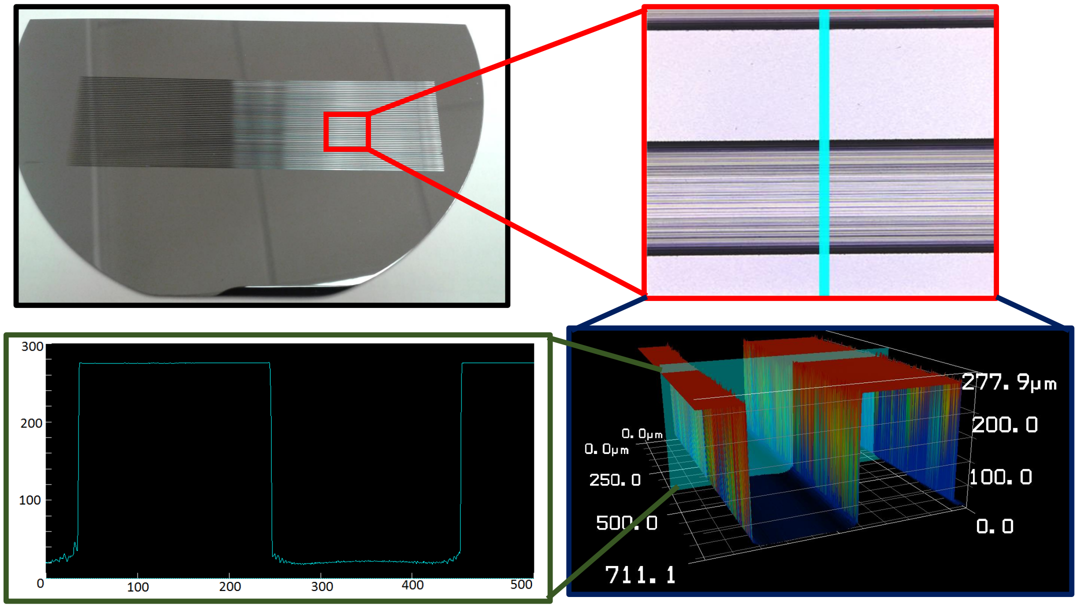

Figure 3.10: Microscope image and profiles of micro-grooves (unit: μm)

In the second trial, the fabrication of micro-grooves (closed ended) has performed. That is dicing saw can move only step by step in vertical direction, and each step size is set by the user. By considering this issue, the initial closed ended micro-grooves are tested with a step size of 50 μm (depth of cut), and it is observed that channel profiles do not have the desired shape and the channel edges had considerable amount of chip removal as shown in Figure 3.9–(b). Moreover, large chip removals are also observed on the diamond saw which reduces the life of the diamond saw dramatically. Therefore, in the light of these findings, in the following trial, micro-grooves are machined with incremental increase in the depth of cut to avoid the edge chip removal. The total height of 200 μm is divided into 10 steps as: $5 + 10 + 20 + 25 + 25 + 25 + 25 + 25 + 20 + 20$ μm. Rotational speed of the dicing blade is set to 30000 rpm with a feed rate of 195.6 mm/min. The fabrication of 50 micro-grooves with the size of 200 μm $\times$ 200 μm $\times$ 75 mm has achieved approximately in 3.5 hours. Microscopic images of micro-grooves can be seen in Figure 3.10. It is clearly seen that micro-groove profiles are perfectly vertical and there is no edge chip removal. One drawback of the dicing saw technique is that due to the circular geometry of the dicing saw, curved profiles has been obtained at the both ends of the micro-grooves. Considering the size of the dicing saw, only about 4 mm portion of the micro-grooves both ends are affected. However, at this point, the effect of the curved sections on the thermal performance of the MHP requires further investigation.

3.1.2.2 High-precision Mechanical Machining

As an alternative to automatic dicing saw, fabrication of micro-grooves by CNC machining with diamond and Polycrystalline Diamond (PCD) cutting tools are also assessed. The used diamond cutting tool (BM0.10R6.0S/0.25 μm product of Counter Fine Tooling) has 100 μm diameter. PCD cutting tool made in house (Micro System Design and Manufacturing Center of Bilkent University). Fabrication is performed by a three-axis CNC milling machine (DECKEL MAHO HSC55, Germany) with HES510-HSKA63 high speed spindle. The cutting tool parameters are listed in Table 3.4. Cutting tools and micro-groove walls are investigated for different cases in which the feed rate, depth of cut of cutting tool and micro-groove depths are changed. For each case, parameters and images are explained below.

Table 3.4: Cutting parameters for diamond tool and PCD cutting tool

	Cutting tool	**Depth of cut** [μm]	**Revolution** [rpm]	**Feed rate** [mm/min]	**Depth** [μm]
Case-A	Diamond	2	25000	30	50
	PCD	2	25000	30	50
Case-B	Diamond	2	25000	10	50
	PCD	2	25000	10	30
Case-C	Diamond	1	25000	10	50
	PCD	1	25000	10	50
Case-D	Diamond	1	25000	30	50
	PCD	1	25000	30	30

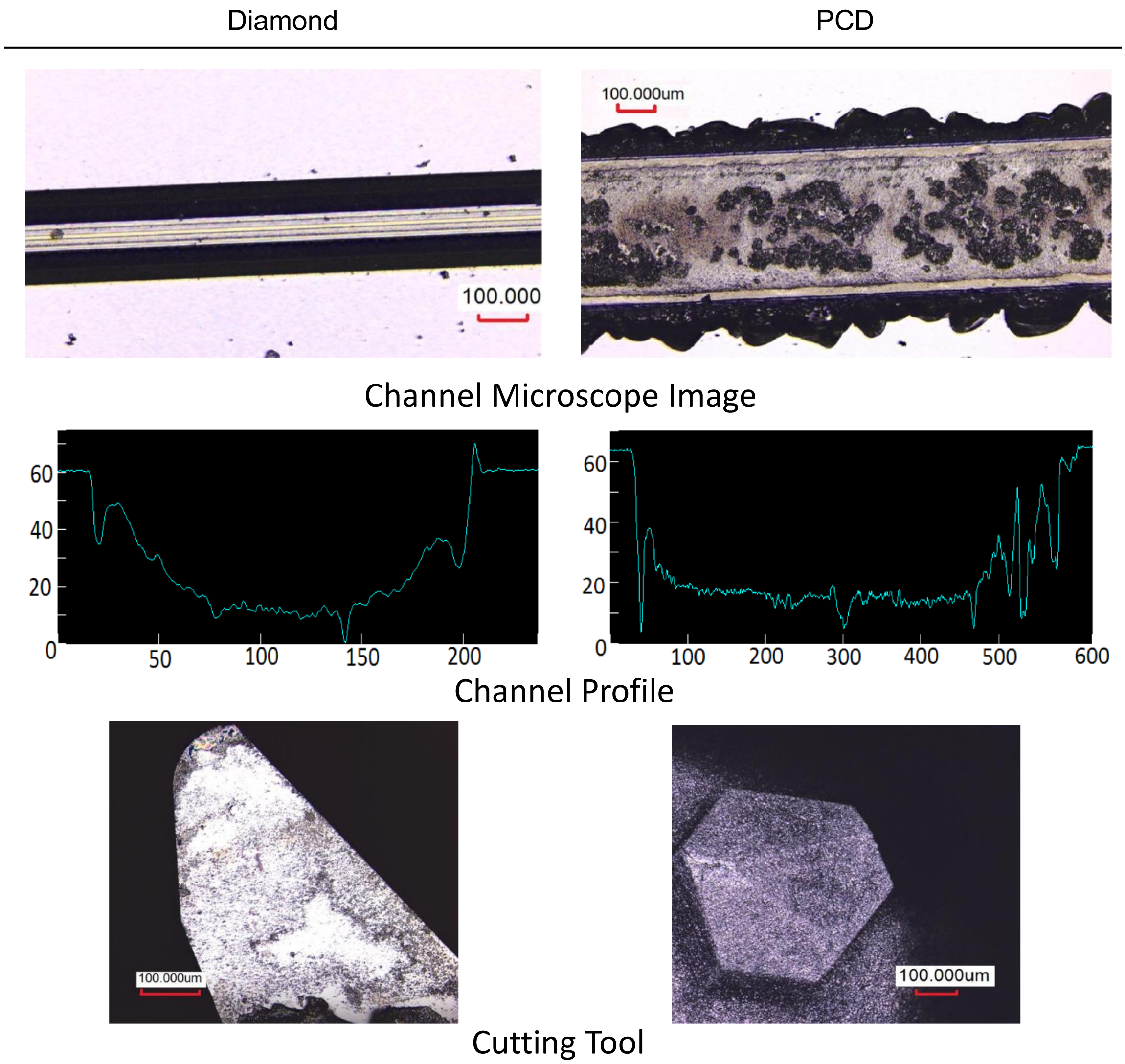

Figure 3.11: Images of micro-grooves and cutting tools (**Case-A**, unit: μm)

In **Case-A** and **Case-B**, the depth of cut is chosen as $2\,\mu$m, and the feed rate is decreased from 30 mm/min to 10 mm/min. The machined depth of the micro-groove is set to $50\,\mu$m (except for PCD tool in **Case-B**). The results for **Case-A** and **Case-B** can be seen in Figures 3.11 and 3.12.

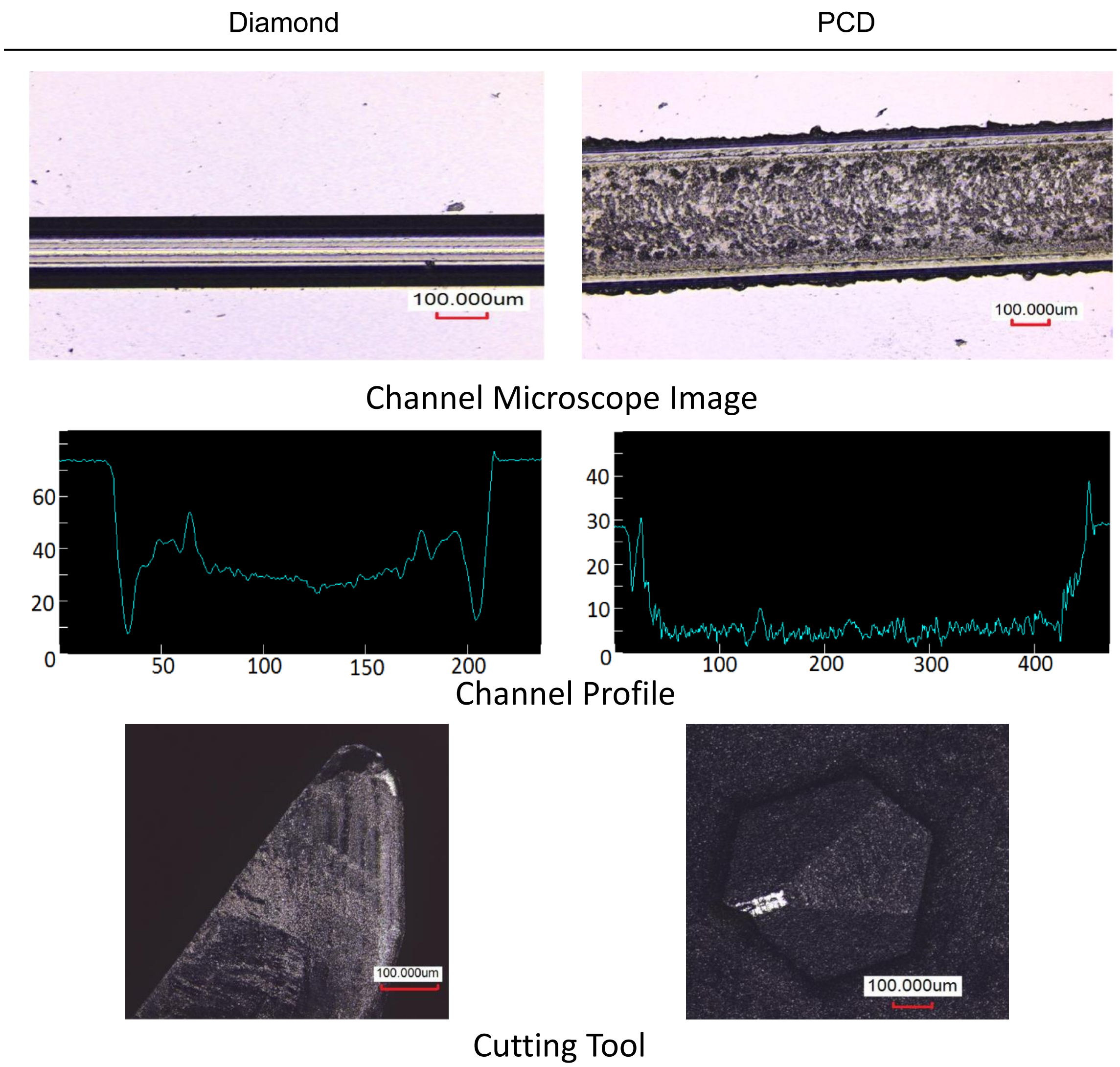

Figure 3.12: Images of micro-grooves and cutting tools (**Case-B**, unit: μm)

Although the edge of the micro-groove is smooth for diamond tool, it is not the case for PCD cutting tool. PCD tool cracks the edge of the micro-groove. That is because the tip of the PCD cutting tool is too small to machine 50 μm depth grooves. Additionally, PCD machined micro-groove has burned silicone chips at the bottom of micro-groove when the feed rate was selected as 30 mm/min. For PCD tool, the cracks at the edge of the micro-groove tend to decrease with the decreasing feed rate as seen in Figure 3.12. From heat transfer point of view, evaporation occurs around the edge of the micro-groove; therefore, these kinds of cracks are not desired in our MHP system. In the case of diamond tool, edge cracks are better, however the groove profile is not rectangular and the surface roughness with a couple of μm exists.

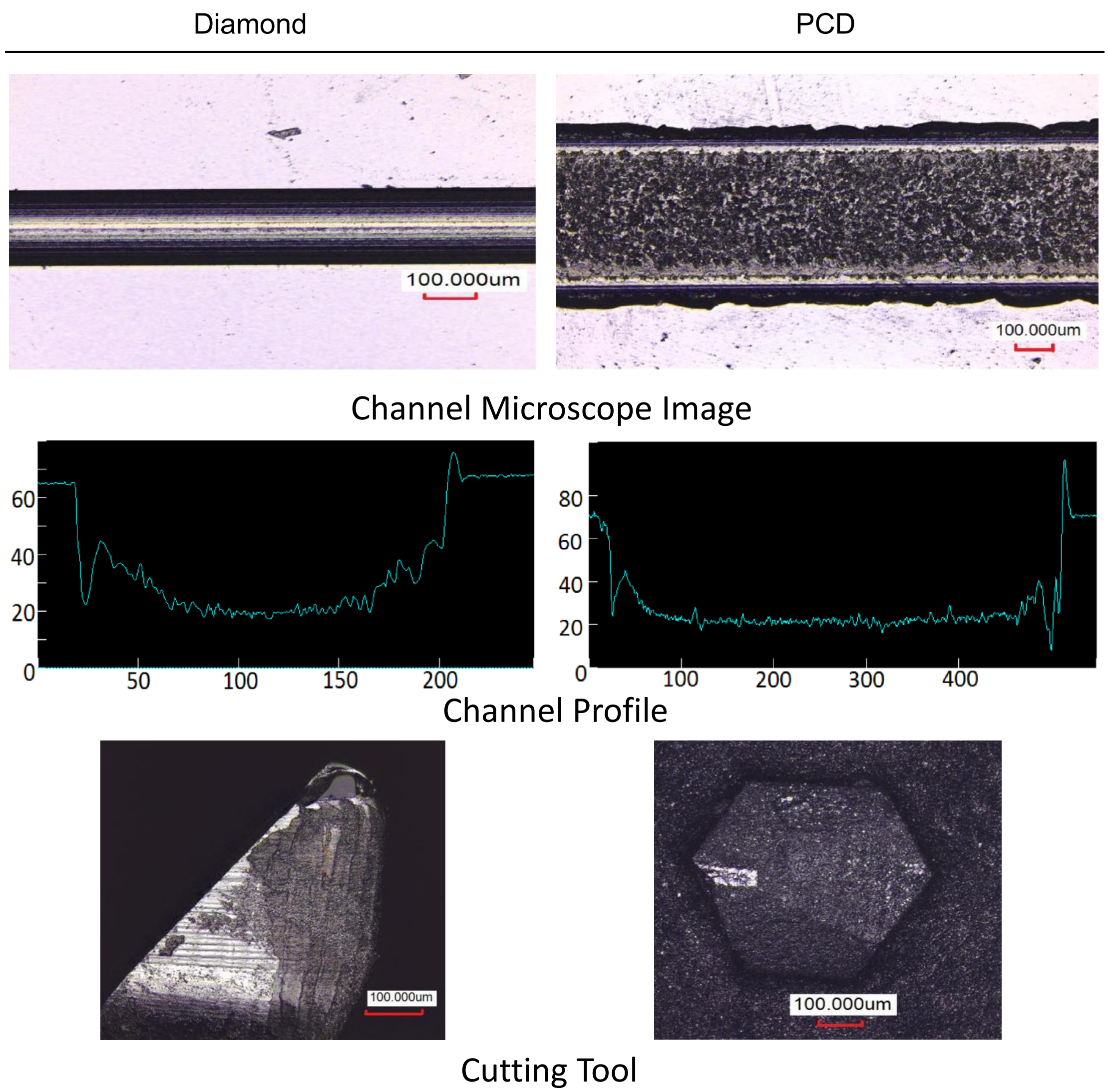

Figure 3.13: Images of micro-grooves and cutting tools (**Case-C**, unit: μm)

In **Case-C** and **Case-D**, the depth of cut is chosen as 1 μm, and the feed rate is set to 10 mm/min and 30 mm/min. The depth of cut is set to 1 μm. The machined depth of the micro-groove is set to 50 μm (except for PCD tool in **Case-D**). The results for **Case-A** and **Case-B** can be seen in Figures 3.13 and 3.14. The edge cracks still exist for the PCD tool. For both cases, the surface roughness tends to decrease, however still in the order of μm, not within the acceptable limit of this study. Both tools fail to achieve a rectangular shape groove.

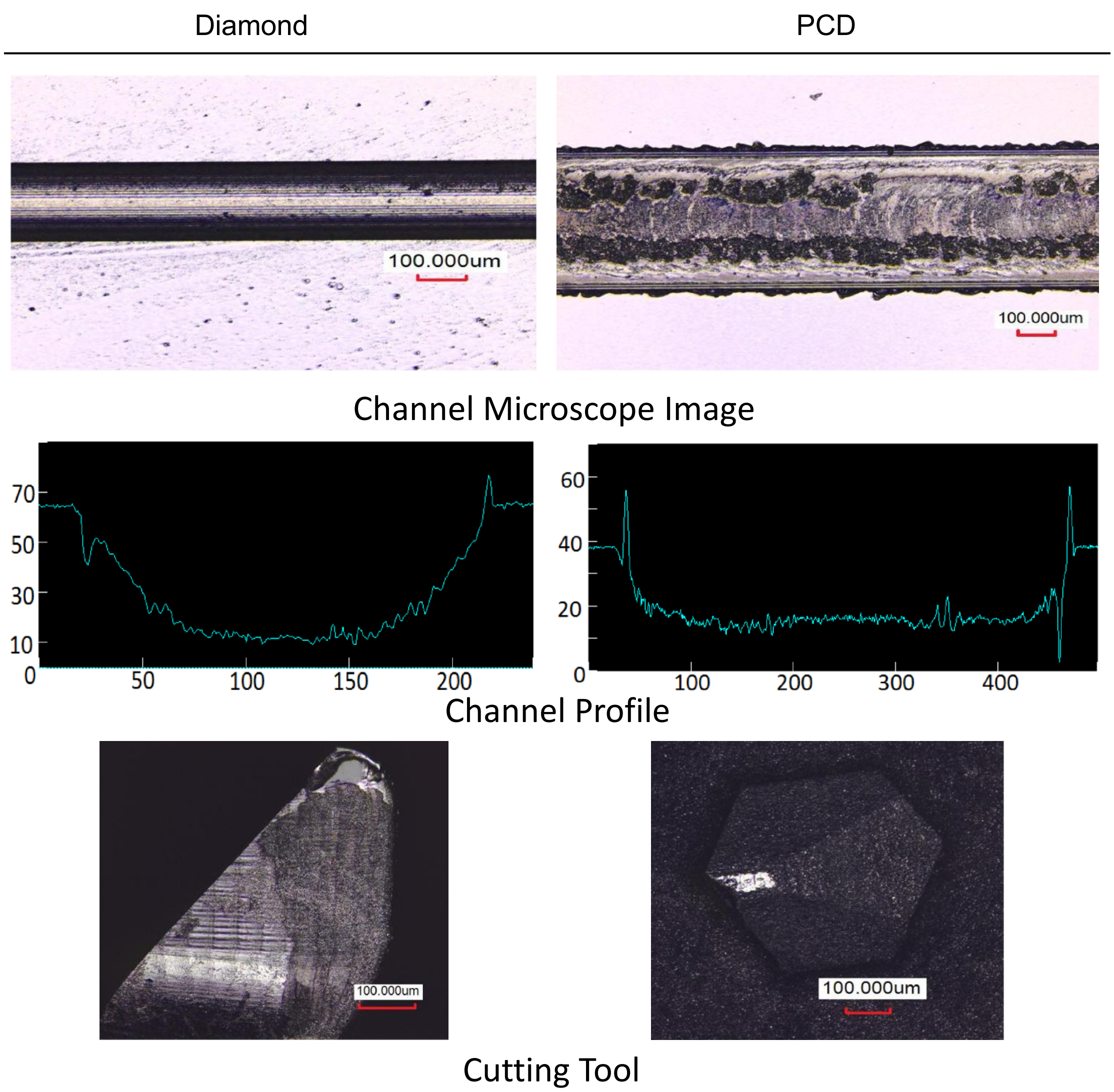

Figure 3.14: Images of micro-grooves and cutting tools (**Case-D**, unit: μm)

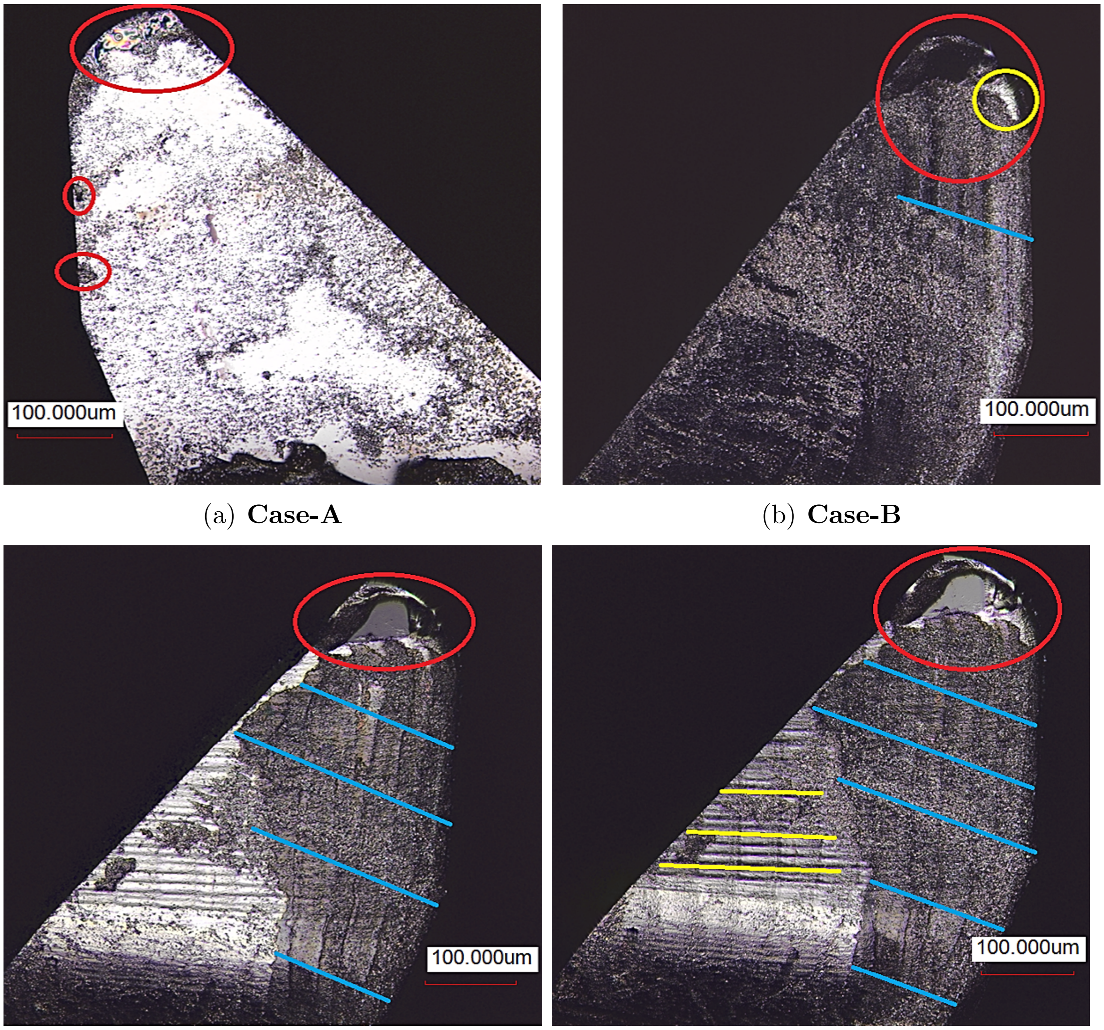

(a) **Case-A** (b) **Case-B**

(c) **Case-C** (d) **Case-D**

Figure 3.15: Images of Diamond cutting tools for each machining

The cutting tools are also investigated under the microscope after each case. The microscope images are shown in Figures 3.15 and 3.16. In the **Case-A**, tip of the diamond cutting tool lost major amount chip (red circle) as it is indicated in Figure 3.15. Then, for each machining process with the same diamond tool, at the same location more chips are removed. Additionally, at side edge of the cutting tools, there starts a new chip removal observed like wavy form (blue and yellow lines). For **Case-A** and **Case-B**, the depth of cut was smaller compared to those of **Case-C** and **Case-D**; therefore, the chip removal on the tip of diamond tool is larger for **Case-A** and **Case-B**.

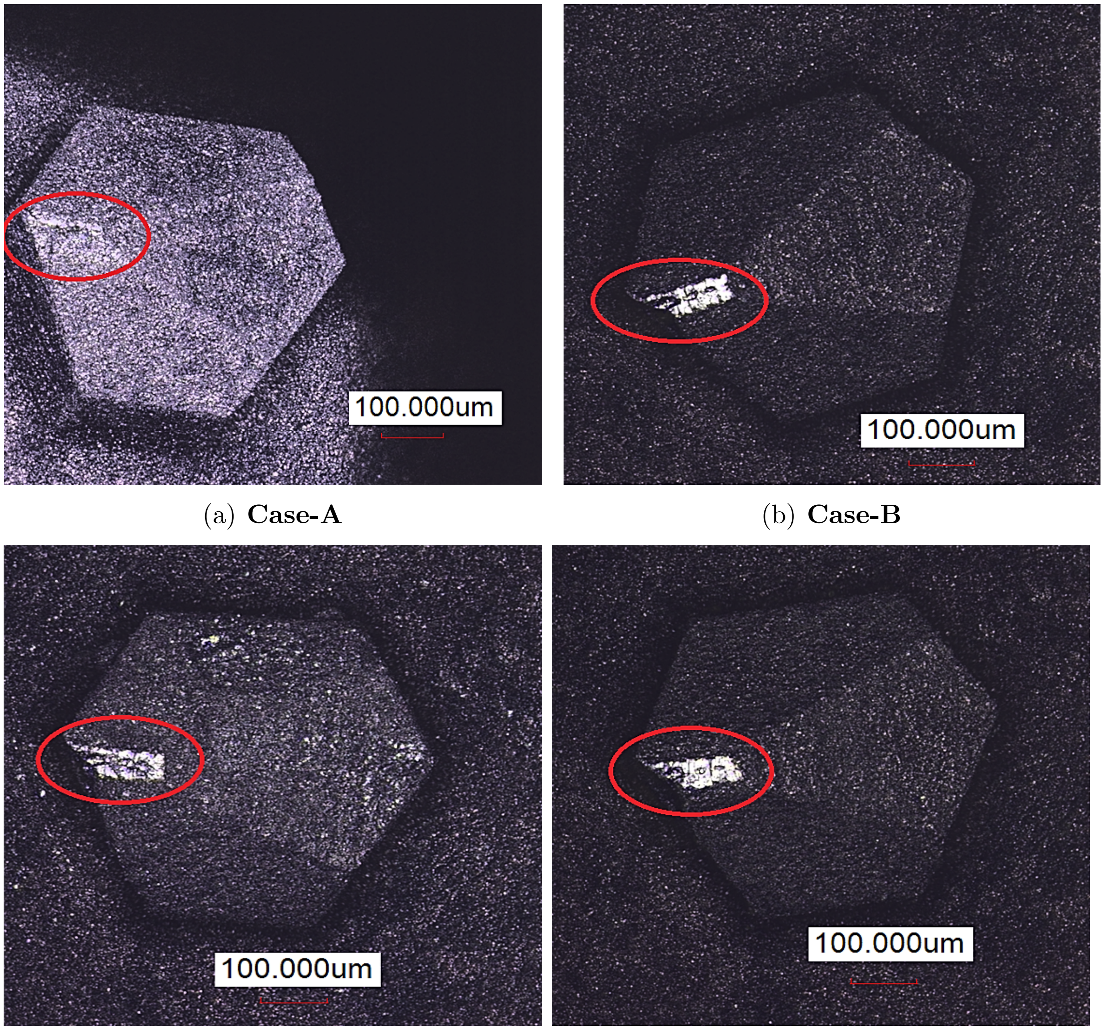

(a) **Case-A** (b) **Case-B**

(c) **Case-C** (d) **Case-D**

Figure 3.16: Images of PCD cutting tools for each machining

In PCD cutting tool, after first machining, there is no significant change as seen in Figure 3.16. However, following the **Case-B**, the chip removal can be seen clearly. Other than that, in **Case-C** and **Case-D**, chip removal on tool is not significant. It can be concluded that there is no major effect of depth of cut and feed rate on the chip removal of PCD cutting tool.

Considering these results, it can be concluded that with suitable diamond cutting tool and with a high-precision machining, the rectangular micro-grooves may be achievable on a silicon wafer with optimized machining parameters. However, for high aspect ration grooves, the machining time would not be feasible considering the depth of cut around 1 μm.

3.1.3 Assessment of Micro-groove Fabrication Techniques

The assessment of the micro-groove fabrication techniques DRIE (Plasma etch), automatic dicing saw and high precision mechanical machining techniques are summarized in Table 3.5 in terms of their ability to fabricate different geometries and sized grooves, total fabrication time, equipment requirements, preliminary additional works and other parameters. One can understand from the table that DRIE process requires some sample preparation steps before etching. These processes basically is photolithography in which photomask, photoresist, developer and mask aligner are needed. Optimized photolithography process for DRIE sample takes about 1.5 hours. Total etching process time for 200 μm depth Si micro-grooves takes around 3.5 hours with including conditioning of DRIE machine (STS- ICP 615). Although it requires additional pre-works, if there is an available cleanroom with the specified requisites, dry etching has more flexibility in etching of any shape micro-groove geometry. The depth of the etching can simply be adjusted by number of cycles in DRIE process. On the other hand, automatic dicing saw only requires dicing blade which is typically $15-20 and dicing saw (dicer). Therefore, it is much cheaper than the dry etching process, however due to the capability of dicer and large diameter of the dicing blade (50 mm), only straight micro-groove manufacturing is feasible. Moreover, at the beginning and end section of the micro grooves, curve featured grooves are generated due to the large diameter of the dicing blade. The estimated curve length in micro-grooves is around 4 mm. The effect of these curvatures on the thermal performance of our MHP system is an open question at this point. If these curvatures are not effective in the system performance, not only the use of dicing saw in straight micro-groove fabrication is very fast (took 3 hours) and easy, but also dicing blade can be used for 2-3 times in the fabrication of 50 micro-grooves. As a last alternative, high-precision CNC machining requires high cost cutting tools (around $2000) which has a certain life. To obtain sharp edges in micro-grooves

Table 3.5: Comparison of different fabrication techniques

	Advantages	Disadvantages
DRIE (Plasma Etch)	• Flexible geometry nm– mm level fabrication • Total fabrication time: 5 hrs (photo-lithography + etching)	• Sample preparation by photolithography • Photoresist, developer, photomask, mask aligner, DRIE machine are required • Cleanroom facility is needed
Automatic Dicing Saw	• Ease of fabrication • Cost effective • 100 μm – mm level fabrication • Total fabrication time: 3 hrs • A dicer machine and a dicing blade are needed	• Only straight channels are possible • Curved features at the beginning and end of a groove due to the circular geometry of the blade
High-precision Mechanical Machining	• Easy fabrication • Flexible geometry • A cutting tool and a high-precision CNC are needed • Total fabrication time (estimated): 200 hrs	• High fabrication cost • Expensive cutting tool • Time consuming • Labor intensive

the depth of cut needs to be low around $1 - 2\,\mu$m which results in approximately 200 hours of machining time for the fabrication of 50 micro-grooves with depth of 200 μm and length of 75 mm. Moreover, it is labor intensive, an operator needs to monitor the machining process throughout out the operation in case of tool break.

3.2 Fabrication of the Cooling Channels

The cooling channels has a cross-section of 2 mm x 2 mm and a total length of 0.19 m. To obtain the required cooling capacity, two set of cooling channels are placed considering flow rate capacity of the syringe pumps used in the experiments. The cooler material selected as PDMS due to the ease of fabrication, flexibility and good bonding with silicon wafer. The cooling channels are fabricated using ODMS molding. The master mold is machined on bronze block. The fabrication of master mold was completed with a three-axis CNC milling machine (DECKEL MAHO HSC55, Germany) with HES510-HSKA63 high speed spindle.

The machined bronze model can be seen Figure 3.17. Following the fabrication of the mold, PDMS molding is performed as follows:

1. Mixing of the polymer and curing agent with a weight ratio of 15:1
2. Degassing the polymer mixture to avoid air trap in the PDMS
3. Pouring PDMS into the master mold and degassing again
4. Baking the mold at 75°C for 90 minutes to cure PDMS
5. Peeling of the PDMS from the mold
6. Punching out the inlet and outlet reservoirs for water
7. Plasma treatment for PDMS and silicon wafer for bonding

The PDMS cooling channels and the microscopic images of the mold can be seen in Figure 3.17 where channel height is $2000 \pm 30\,\mu$m with a space of 1 mm between channels.

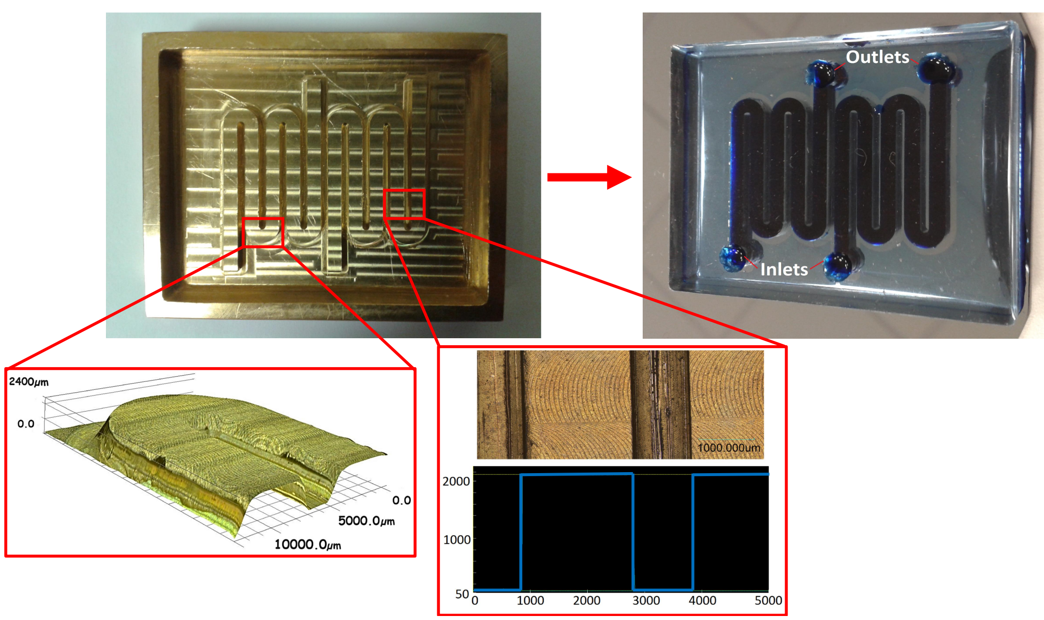

Figure 3.17: Microcope image of the fabricated cooling channels (unit: μm)

3.3 Fabrication of the Heater

Cr is coated on silicon wafer with using sputtering which is a thin film deposition technique. Main procedures in fabrication of Cr heater are photolithography and sputtering. Geometry of the Cr heater is first printed on an acetate paper for masking in photolithography. The photolithography steps are as follows:

1. Cleaning silicone wafer with acetone, isopropanol and pure water
2. Spin coating of HMDS (Hexamethyldisilazane) on silicone wafer with spin coater (revolution of 4000 rpm, 40 sec, acceleration of 1088 rpm/s)
3. Spin coating AZ 5214 E photoresist on Si wafer with revolution of 2000 rpm, 30 sec, acceleration of 408 rpm/s
4. Prebaking photoresist for (5 min at room temperature, 1 min at 80°C and 1 min at 110°C)
5. Cooling photoresist coated sample at room temperature for 5 min
6. Cleaning of acetate mask with acetone, isopropanol and pure water
7. UV light exposure with dose of 400 mJ/cm^2 with using EVG 620 Automated Mask Alignment System
8. Immersion of the sample in AZ 400K diluted with pure water (1:4 volume ratio) for 7 min
9. Post baking (1 min at 80 °C and 2 min at 120 °C)
10. Cooling down at room temperature for 10 min

After photolithography process, sample 500 nm Cr coated with sputtering technique by using Leybold L-560 box coater. Sample is placed into the acetone to remove the photoresist, and is cleaned with DI water. Cr coated Si wafer is represented in Figure 3.18–(a). The connection cables are glued onto the connection pads with the conductive glue as shown in Figure 3.18–(b).

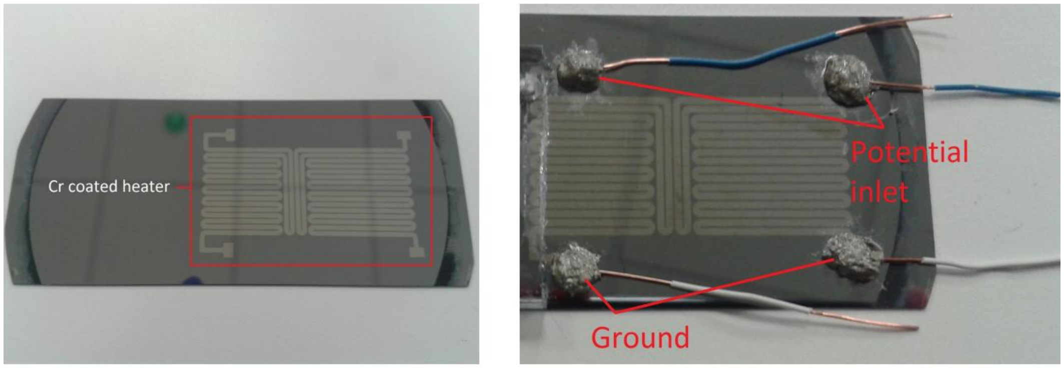

(a) Cr coated heater on Si wafer

(b) Connection of electric cables with conductive epoxy

Figure 3.18: Photograph of the fabricated Cr heater

3.4 Assembly of the MHP System

Following the fabrication of the components, the assembly of the system is performed. The overall fabrication cycle together with the assembly operation of components (Si micro-grooves MHP, PDMS cooler, Cr heater, PDMS bonder and fused silica with inlet outlet ports) can be listed as follows:

1. Fabrication of micro-grooves on Si wafer with DRIE and automatic dicing saw
2. Cr coating of Si wafer with sputtering
3. PDMS cooler and bonder fabrication
4. Fused silica hole preparation with laser machining
5. Assembly of parts with plasma cleaner
6. Connection of copper cables with conductive epoxy
7. Connection of inlet-outlet ports with epoxy

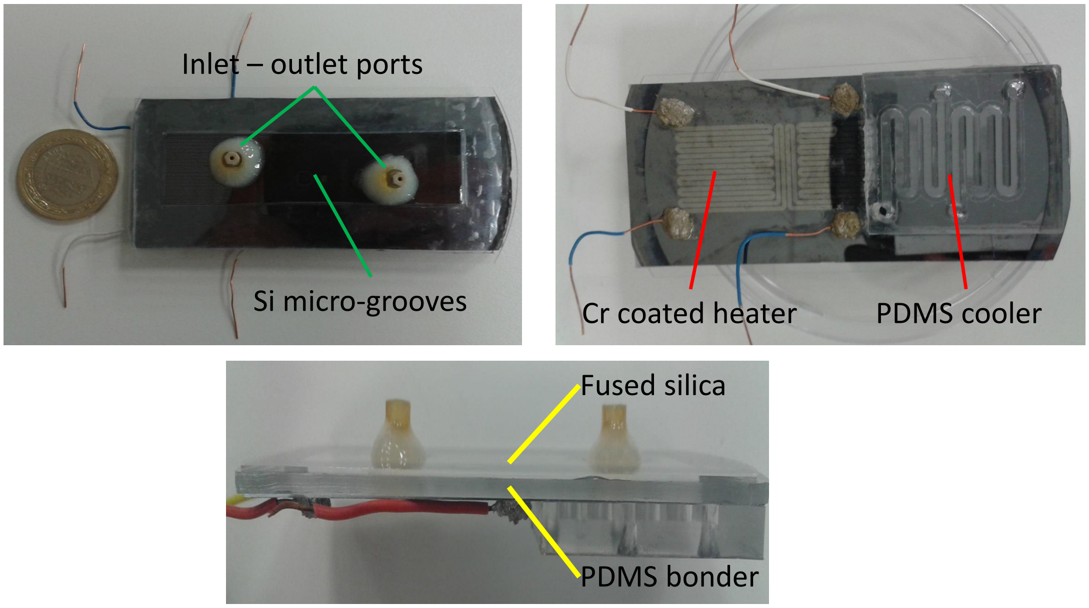

Figure 3.19: Photograph of the final Si micro-grooved heat pipe system

Assembled MHP system from top, bottom, front views are presented in Figure 3.19. 50 micro-grooves on Si wafer fabricated with DRIE, inlet and outlet ports on fused silica, Cr coated heater, PDMS cooler, fused silica and PDMS bonder are indicated on the figure.

Chapter 4

Concluding Remarks

MHPs are the most promising cooling devices for many application areas in micro and mini levels such as cooling of IC circuit, microchips and LEDs. This is due to fact that large amount of thermal energy is transferred from one phase to another during the phase change of a working fluid. Additionally, the simplicity, no additional component requirements are the other advantages of MHPs. Therefore, a MHP system is designed according to computational models and fabricated with the determined parameters of the MHP system. A 3-D Multiphysics computational model is developed to realize the 3-D effects and temperature distribution on a complete MHP system which will be used to verify the UCM (Unit-Cell-Model) experimentally. From this study, the following conclusions and remarks can be summarized as:

- Computational model has developed for a complete MHP system with using COMSOL Multiphysics program. The necessary heat transfer coefficient data at evaporator and condenser region, constant heat transfer coefficient at cooler region and heat transfer rate in heater region are obtained from UCM. The complete MHP system consists of 50 of 200 μm $\times$ 200 μm $\times$ 75 mm micro-grooves on 4'' silicon wafer together with Cr coated heaters, PDMS cooler, PDMS bonder and fused silica cover. The overall energy balance on the MHP system is simulated and the resultant heat rates and temperature distributions are analyzed. The temperature distribution along the edges of MHP grooves are compared with UCM results. The results exhibits a similar trend however there exists a discrepancy mainly due to the 3-D conduction heat transfer through the Si wafer. The heat transfer rates obtained in 3-D model and UCM are analyzed and it is concluded that heat transfer rates are closer to each other at condenser and evaporator sections in UCM where the vapor temperature is 321.8 K. When the 3-D simulation applied for this vapor temperature, it is observed that the heat transfer rates in evaporator and condenser sections are equal and deviate from the results of UCM due to 3-D heat conduction effects in MHP. Therefore, the equivalence of condenser and evaporator heat rates are obtained with changing vapor temperature inside the system which is determined as 320.1 K. For that case the condenser and evaporator heat rates are determined as 7.57 W and 7.57 W and the error between two values is found to be less than 1%.

- Lithography-based and mechanical-based fabrication techniques are tested for the square micro-groove MHPs on Si wafer. In lithography-based fabrication, dry etching process is performed to fabricate micro-grooves with anisotropic micro-groove walls. Photolithography process has been completed on a 4'' Si wafer with a DRIE recipe developed in this work. The preferred depth of micro-groove (200 μm) is obtained for 580 cycle of dry etching process with grassing which is below 5% (acceptable) of micro-groove height. In mechanical-based fabrication, cutting tools with high precision mechanical machining and automatic dicing saw are used. Diamond and PCD cutting tools are tested in high-precision mechanical machining. It is observed that neither diamond tool nor the PCD tool show a satisfactory results in terms of surface roughness and vertical side walls. Moreover, high precision mechanical machining has turned out to be unfeasible process in terms time and the cost to fabricate micro-grooves. In contrary to high-precision mechanical machining, satisfactory results have been achieved by dicing saw. The only disadvantage of dicing saw is the curve-shaped profile at the end of the grooves. However, it has been observed that the dicing saw technique has turned out to be extremely fast and cost effective method compare to dry etching and high precision mechanical machining techniques.

As future work, the fabricated MHP system will be used in the experiments to verify the consistency between computational model with experiments. This procedure will also enable the verification of the UCM which is the base computational model which feeds heat transfer coefficient data for the developed computational model. Having successfully completed the verification process, the implementation of the silicon-based micro-groove heat pipe for the cooling of a real electronic circuit architecture will be ultimate goal this research.

Bibliography

[1] H. N. Chaudhry, B. R. Hughes, and S. A. Ghani, "A review of heat pipe systems for heat recovery and renewable energy applications," *Renewable and Sustainable Energy Reviews*, vol. 16, no. 4, pp. 2249–2259, 2012.

[2] M. C. Zaghdoudi, S. Maalej, J. Mansouri, and M. B. H. Sassi, "Flat miniature heat pipes for electronics cooling: State of the art, experimental and theoretical analysis," *World Academy of Science, Engineering and Technology*, vol. 51, pp. 879–902, 2011.

[3] F. Incropera, D. DeWitt, T. Bergman, and A. Lavine, *Fundamentals of Heat and Mass Transfer*, p. 519. Wiley, 2007.

[4] A. Aydemir, "Deep-trench rie optimization for high performance mems microsensors," Master's thesis, Middle East Technical University, Turkey, August 2007.

[5] K. E. G. L. Zhang and T. W. Kenny, *Silicon Microchannel Heat Sinks Theories and Phenomena*, pp. 1–11. Springer-Verlag Berlin Heidelberg, 2004.

[6] D. Zhao and G. Tan, "A review of thermoelectric cooling: Materials, modeling and applications," *Applied Thermal Engineering*, vol. 66, no. 1–2, pp. 15 – 24, 2014.

[7] A. Bar-Cohen, M. Arik, and M. Ohadi, "Direct liquid cooling of high flux micro and nano electronic components," *Proceedings of the IEEE*, vol. 94, no. 8, pp. 1549–1570, 2006.

[8] J. Kim, "Spray cooling heat transfer: The state of the art," *International Journal of Heat and Fluid Flow*, vol. 28, no. 4, pp. 753 – 767, 2007.

[9] L. Jiang, M. Wong, and Y. Zohar, "Forced convection boiling in a microchannel heat sink," *Microelectromechanical Systems, Journal of*, vol. 10, no. 1, pp. 80–87, 2001.

[10] B. Suman, "Modeling, experiment, and fabrication of micro-grooved heat pipes: An update," *Applied Mechanics Reviews*, vol. 60, no. 3, pp. 107–119, 2007.

[11] G. Odabasi, *Modeling of Multidimensional heat transfer in a rectangular grooved heat pipe*. PhD thesis, Middle East Technical University, Turkey, June 2014.

[12] P. Nemec, A. Čaja, and M. Malcho, "Mathematical model for heat transfer limitations of heat pipe," *Mathematical and Computer Modelling*, vol. 57, no. 1–2, pp. 126–136, 2013.

[13] B. Kim and G. Peterson, "Analysis of the critical weber number at the onset of liquid entrainment in capillary-driven heat pipes," *International Journal of Heat and Mass Transfer*, vol. 38, no. 8, pp. 1427–1442, 1995.

[14] T. P. Cotter, "Principles and prospects of micro heat pipes," in *Proceedings of the 5th Int. Heat Pipe Conference, Tsukuba, JAPAN*, pp. 328–332, 1984.

[15] AMECThermasol, "Flat cool pipes – mhp series." `http://www.amecthermasol.co.uk/datasheets/MHP_Full_Data.pdf`, March 2015.

[16] D. A. Reay, P. A. Kew, R. McGlen, and P. D. Dunn, *Heat pipes: Theory, Design, and Applications*, pp. 65–72. Butterworth-Heinemann, 2014.

[17] F. L. Chang and Y. M. Hung, "The coupled effects of working fluid and solid wall on thermal performance of micro heat pipes," *International Journal of Heat and Mass Transfer*, vol. 73, no. 0, pp. 76 – 87, 2014.

[18] C. B. Sobhan, R. L. Rag, and G. P. Peterson, "A review and comparative study of the investigations on micro heat pipes," *International Journal of Energy Research*, vol. 31, no. 6–7, pp. 664–688, 2007.

[19] X. Liu and Y. Chen, "Transient thermal performance analysis of micro heat pipes," *Applied Thermal Engineering*, vol. 58, no. 1–2, pp. 585–593, 2013.

[20] D. Sugumar and K.-K. Tio, "The effects of working fluid on the heat transport capacity of a microheat pipe," *Journal of Heat Transfer*, vol. 131, no. 1, p. 012401, 2008.

[21] Z.-H. Liu, J.-G. Xiong, and R. Bao, "Boiling heat transfer characteristics of nanofluids in a flat heat pipe evaporator with micro-grooved heating surface," *International Journal of Multiphase Flow*, vol. 33, no. 12, pp. 1284 – 1295, 2007.

[22] X. F. Yang, Z.-H. Liu, and J. Zhao, "Heat transfer performance of a horizontal micro-grooved heat pipe using cuo nanofluid," *Journal of Micromechanics and Microengineering*, vol. 18, no. 3, p. 035038, 2008.

[23] J. Qu, H. Wu, and P. Cheng, "Start-up, heat transfer and flow characteristics of silicon-based micro pulsating heat pipes," *International Journal of Heat and Mass Transfer*, vol. 55, no. 21–22, pp. 6109 – 6120, 2012.

[24] M. Rahmat and P. Hubert, "Two-phase simulations of micro heat pipes," *Computers & Fluids*, vol. 39, no. 3, pp. 451–460, 2010.

[25] Y. M. Hung and Q. Seng, "Effects of geometric design on thermal performance of star-groove micro-heat pipes," *International Journal of Heat and Mass Transfer*, vol. 54, no. 5–6, pp. 1198–1209, 2011.

[26] S.-W. Chen, J.-C. Hsieh, C.-T. Chou, H.-H. Lin, S.-C. Shen, and M.-J. Tsai, "Experimental investigation and visualization on capillary and boiling limits of micro-grooves made by different processes," *Sensors and Actuators A: Physical*, vol. 139, no. 1–2, pp. 78–87, 2007.

[27] R. Rullière, F. Lefèvre, and M. Lallemand, "Prediction of the maximum heat transfer capability of two-phase heat spreaders - experimental validation," *International Journal of Heat and Mass Transfer*, vol. 50, no. 7–8, pp. 1255–1262, 2007.

[28] H. T. Lim, S. H. Kim, H. D. Im, K. H. Oh, and S. H. Jeong, "Fabrication and evaluation of a copper flat micro heat pipe working under adverse-gravity orientation," *Journal of Micromechanics and Microengineering*, vol. 18, no. 10, p. 105013, 2008.

[29] R. Revellin, R. Rullière, F. Lefèvre, and J. Bonjour, "Experimental validation of an analytical model for predicting the thermal and hydrodynamic capabilities of flat micro heat pipes," *Applied Thermal Engineering*, vol. 29, no. 5–6, pp. 1114–1122, 2009.

[30] F. Lefèvre, R. Rullière, S. Lips, and J. Bonjour, "Confocal microscopy for capillary film measurements in a flat plate heat pipe," *Journal of Heat Transfer*, vol. 132, p. 6, 2010.

[31] S. Lips, F. Lefèvre, and J. Bonjour, "Combined effects of the filling ratio and the vapour space thickness on the performance of a flat plate heat pipe," *International Journal of Heat and Mass Transfer*, vol. 53, no. 4, pp. 694 – 702, 2010.

[32] S. Lips, F. Lefèvre, and J. Bonjour, "Physical mechanisms involved in grooved flat heat pipes: Experimental and numerical analyses," *International Journal of Thermal Sciences*, vol. 50, no. 7, pp. 1243–1252, 2011.

[33] Y. Tang, Z. Hu, J. Qing, Z. Xie, T. Fu, and W. Chen, "Experimental investigation on isothermal performance of the micro-grooved heat pipe," *Experimental Thermal and Fluid Science*, vol. 47, no. 0, pp. 143–149, 2013.

[34] X. Li, J. Wang, Q. Hu, L. Bao, and H. Zhang, "Experimental and theoretical research on capillary limit of micro heat pipe with compound structure of sintered wick on trapezium-grooved substrate," *Heat and Mass Transfer*, vol. 49, pp. 381–389, 2013.

[35] A. J. Jiao, H. B. Ma, and J. K. Critser, "Evaporation heat transfer characteristics of a grooved heat pipe with micro-trapezoidal grooves," *International Journal of Heat and Mass Transfer*, vol. 50, no. 15–16, pp. 2905 – 2911, 2007.

[36] K. H. Do, S. J. Kim, and S. V. Garimella, "A mathematical model for analyzing the thermal characteristics of a flat micro heat pipe with a grooved wick," *International Journal of Heat and Mass Transfer*, vol. 51, no. 19–20, pp. 4637–4650, 2008.

[37] J. Qu, H. Wu, and P. Cheng, "Effects of functional surface on performance of a micro heat pipe," *International Communications in Heat and Mass Transfer*, vol. 35, no. 5, pp. 523 –528, 2008.

[38] X. Wang, T. Yong, and C. Ping, "Investigation into performance of a heat pipe with micro grooves fabricated by extrusion–ploughing process," *Energy Conversion and Management*, vol. 50, no. 5, pp. 1384 –1388, 2009.

[39] Y. M. Hung and K.-K. Tio, "Analysis of microheat pipes with axial conduction in the solid wall," *Journal of Heat Transfer*, vol. 132, no. 7, p. 071301, 2010.

[40] Y. M. Hung and K.-K. Tio, "Thermal analysis of optimally designed inclined micro heat pipes with axial solid wall conduction," *International Communications in Heat and Mass Transfer*, vol. 39, no. 8, pp. 1146–1153, 2012.

[41] K.-K. Tio and Y. M. Hung, "Analysis of overloaded micro heat pipes: Effects of solid thermal conductivity," *International Journal of Heat and Mass Transfer*, vol. 81, no. 0, pp. 737–749, 2015.

[42] S. Taze, B. Çetin, and Z. Dursunkaya, "Multi-physics modeling of silicon micro-grooved heat pipe," in *Proceedings of 8th International Conference on Computational Heat and Mass Transfer, İstanbul, TURKEY*, May 2015.

[43] J. Quero, F. Perdigones, and C. Aracil, "10 - microfabrication technologies used for creating smart devices for industrial applications," in *Smart Sensors and Mems*, pp. 281–304, Woodhead Publishing, 2014.

[44] M. J. Madou, *Fundamentals of microfabrication : the science of miniaturization*, pp. 2–5. Boca Raton : CRC Press, 2002.

[45] J. X. Zhang and K. Hoshino, "Chapter 2 - fundamentals of nano/micro-fabrication and effect of scaling," in *Molecular Sensors and Nanodevices*, pp. 43–101, Oxford: William Andrew Publishing, 2014.

[46] F. Laermer, S. Franssila, L. Sainiemi, and K. Kolari, "Chapter twenty three - deep reactive ion etching," in *Handbook of Silicon Based {MEMS} Materials and Technologies*, pp. 349–374, Boston: William Andrew Publishing, 2010.

Appendix A

Heat Transfer Coefficient Calculations

Calculation steps of the heat transfer coefficient on the bottom surface of the fused silica cover:

Heat transfer coefficient calculation of spacing (Space between fused silica and PDMS)

Known:

V_{vapor} = 250 mm/s
T_{vapor} ≅ 320.7 K
P_{vapor} = 0.10 bar
L_{space} = 75 mm

Calculation	**Property data [41]**
$Re = \frac{\rho V_{vapor} L_{space}}{\mu} = \frac{0.07153\,\frac{\text{kg}}{\text{m}^3} * 0.25\,\frac{m}{s} * 0.075\,m}{9.89\text{x}10^{-6}\ \text{N.s/m}^2} = 135$	ρ = 0.07153 kg/m^3 μ = 9.89x10^{-6} N.s/m^2
$\overline{Nu}_L = 0.664\, Re_L^{1/2}\, Pr^{1/3} = 0.664 * 135^{1/2} * 0.894^{1/3} = 7.43$	Pr = 0.894
$\bar{h} = \frac{\overline{Nu}_L\, k}{L_{space}} = \frac{7.43 * 21\, W/m.K}{0.075\, m} = 2081\,\frac{W}{m^2.K}$	k = 21 W/m.K

Calculation steps of the heat transfer coefficient on the cooling channel walls for fully-developed laminar flow:

Heat transfer coefficient calculation of cooler channel walls

Known:

ΔT = 1 K (Inlet- Exit temperature difference)
$a \; x \; b$ = 2 mm x 2 mm (Cooling channel size)
Q_{cooler} = 8.978 W (Cooler heat removal rate)

Material properties are taken for 300 K that is close to mean of inlet and exit temperature of the water in cooling channels

Calculation	**Property data [41] for T_{mean}= 300 K**
$Q_{cooler} = \dot{m} c_p \Delta T$ $\dot{m} = \frac{\mathrm{Q_{cooler}}}{c_p \Delta T} = \frac{8.978 \text{ W}}{4186 \frac{J.kg}{K} * 1K} = 0.0011 \; kg/s$	c_p = 4186 J.kg/K
$A = a \; x \; b = 2 \; mm * 2 \; mm = 4 \; x \; 10^{-6} \; m^2$ $V = \frac{\dot{m}}{\rho A} = \frac{0.0011 \; kg/s}{998 \frac{kg}{m^3} * 4 \; x \; 10^{-6} \; m^2} = 0.2686 \; m/s$ $\dot{V} = VA = 0.2686 \frac{m}{s} * 4 \; x \; 10^{-6} \; m^2 = 1.0745 \; x \; 10^{-6} \frac{m^3}{s}$ $= 1.0745 \; x \; 10^{-6} \frac{m^3}{s} * \frac{10^6 mL}{m^3} * \frac{60 \; s}{min} = 64.47 \frac{mL}{min}$	$\rho = 998 \; kg/m^3$
$D_h = \frac{4A}{P} = \frac{4 \; (a \; x \; b)}{2(a+b)} = a = 2 \; x \; 10^{-3} \; m$ $Re = \frac{\rho V D_h}{\mu} = \frac{998 \frac{kg}{m^3} * \; 0.2686 \frac{m}{s} * \; 2 \; x \; 10^{-3} \; m}{1 \; x \; 10^{-3} \frac{kg}{s.m}} = 536.2$ $Nu = 2.98 \; for \; \frac{b}{a} = \frac{2 \; mm}{2 \; mm} = 1$ $h = \frac{Nu \; k}{D_h} = \frac{2.98 * 0.6 \frac{W}{m.K}}{2 \; x \; 10^{-3} \; m} = 894.0 \frac{W}{m^2.K}$	$\mu = 1 \; x \; 10^{-3} \frac{kg}{s.m}$ $k = 0.6 \frac{W}{m.K}$

The other fully developed laminar flow Nu numbers are calculated with using curve fitting between Nu number and b/a ratio. The curve fit uses 5 degree of polynomial for the range of 1-4 of b/a ratio to obtain best fitted data in this range.

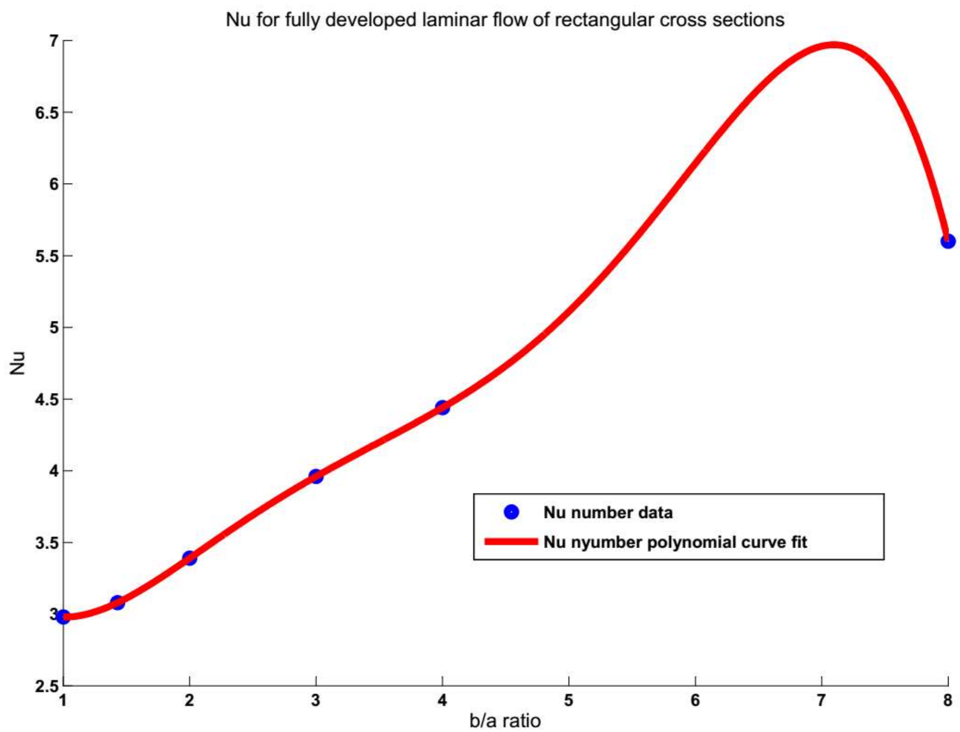

Appendix B

Heat Transfer Coefficient Data

The heat transfer coefficient data along the 75-mm micro-grooved heat pipe from the detailed computational model of [11] for the unit-cell:

Evaporator side			Condenser side			Condenser side cont.		
y	Twall (K)	h ($W/m^2.K$)	y	Twall (K)	h ($W/m^2.K$)	y	Twall (K)	h ($W/m^2.K$)
0.00000	320.74	3413.68	0.03000	321.92	28643.85	0.06075	325.57	15966.62
0.00075	320.86	36517.46	0.03075	322.46	16815.25	0.06150	325.57	15992.11
0.00150	320.90	36357.61	0.03150	322.93	15644.10	0.06225	325.56	16009.18
0.00225	320.93	36233.42	0.03225	323.34	15261.55	0.06300	325.56	16025.80
0.00300	320.94	36130.70	0.03300	323.69	15082.21	0.06375	325.55	16043.68
0.00375	320.95	36048.04	0.03375	323.99	14994.37	0.06450	325.55	16061.31
0.00450	320.96	35970.34	0.03450	324.24	14954.48	0.06525	325.55	16070.12
0.00525	320.96	35896.25	0.03525	324.46	14944.68	0.06600	325.55	16088.14
0.00600	320.96	35817.47	0.03600	324.65	14952.21	0.06675	325.54	16102.26
0.00675	320.96	35741.01	0.03675	324.81	14958.69	0.06750	325.54	16113.51
0.00750	320.96	35661.99	0.03750	324.95	14989.44	0.06825	325.54	16113.25
0.00825	320.96	35573.31	0.03825	325.06	15013.86	0.06900	325.54	16128.81
0.00900	320.96	35480.65	0.03900	325.16	15043.50	0.06975	325.53	16130.53
0.00975	320.96	35379.37	0.03975	325.24	15078.55	0.07050	325.53	16148.46
0.01050	320.96	35275.09	0.04050	325.31	15114.65	0.07125	325.53	16154.66
0.01125	320.95	35161.67	0.04125	325.37	15146.81	0.07200	325.53	16159.24
0.01200	320.95	35037.99	0.04200	325.42	15178.25	0.07275	325.53	16156.78
0.01275	320.95	34911.71	0.04275	325.46	15225.03	0.07350	325.53	16166.42
0.01350	320.95	34778.09	0.04350	325.49	15261.33	0.07425	325.53	16165.05
0.01425	320.94	34636.72	0.04425	325.52	15293.52	0.07500	325.53	16163.96
0.01500	320.94	34487.18	0.04500	325.54	15337.50			
0.01575	320.94	34332.99	0.04575	325.56	15368.43			
0.01650	320.93	34173.28	0.04650	325.58	15411.33			
0.01725	320.93	34006.73	0.04725	325.59	15448.99			
0.01800	320.92	33835.27	0.04800	325.59	15476.24			
0.01875	320.92	33651.88	0.04875	325.60	15516.99			
0.01950	320.92	33467.33	0.04950	325.60	15554.45			
0.02025	320.91	33274.06	0.05025	325.61	15589.06			
0.02100	320.91	33072.15	0.05100	325.61	15621.17			
0.02175	320.91	32859.33	0.05175	325.61	15654.75			
0.02250	320.91	32635.26	0.05250	325.61	15685.76			
0.02325	320.91	32396.50	0.05325	325.60	15712.99			
0.02400	320.92	32136.24	0.05400	325.60	15737.10			
0.02475	320.93	31839.35	0.05475	325.60	15775.71			
0.02550	320.96	31484.26	0.05550	325.60	15803.36			
0.02625	321.00	31029.58	0.05625	325.59	15822.27			
0.02700	321.06	30368.88	0.05700	325.59	15854.15			
0.02775	321.15	29214.90	0.05775	325.58	15872.89			
0.02850	321.31	26480.13	0.05850	325.58	15905.60			
0.02925	321.54	13531.80	0.05925	325.58	15928.65			
			0.06000	325.57	15940.18			